Atmospheric
Chemistry
and Physics
Discussions

Open Access

1

1 **Examination of effects of aerosols on a pyroCb and their dependence on fire**
2 **intensity and aerosol perturbation using a cloud-system resolving model**

3

4

5 Seoung Soo Lee[1], George Kablick III[2,3], Zhanqing Li[2]

6

7 [1]Research Foundation, San Jose State University, San Jose, California, USA

8 [2]Earth System Science Interdisciplinary Center, University of Maryland, College Park,

9 Maryland, USA

10 [3]US Naval Research Laboratory, Washington, DC, USA

11

12

13

14

15

16

17

18

19

20

21

22

23

24

25 **Abstract**

26

27 This study investigates how a pyrocumulonimbus (pyroCb) event influences water vapor

28 concentrations and cirrus cloud properties near the tropopause, specifically focusing on

29 how fire-produced aerosols affect this role via a modeling framework. Results from a case

30 study show that when observed fire intensity is high, there is an insignificant impact of

31 fire-produced aerosols on the convective development of the pyroCb and associated

32 changes in water vapor and the amount of cirrus cloud near the tropopause. However, as

33 fire intensity weakens, the effects of aerosols on microphysical variables and processes

34 such as droplet size and autoconversion increase. Modeling results shown herein indicate

35 that aerosol-induced invigoration of convection is significant for pyroCb with weak-

36 intensity fires and associated weak surface heat fluxes. Thus, there is a greater aerosol

37 effect on the transportation of water vapor to the upper troposphere and the production of

38 cirrus cloud with weak-intensity fires, whereas these effects are muted with strong-

39 intensity fires.

40

41

42

43

44

45

46

47

48

49

50

51

52

53

54

55

Atmospheric
Chemistry
and Physics
Discussions

1. Introduction

56

57

58   A recent study by Kablick et al. (2018) has shown that pyrocumulonimbus (pyroCbs) can

59   transport significant amounts of water vapor to the upper troposphere and the lower

60   stratosphere (UTLS) and thus may have a role in seasonal UTLS water vapor budgets. Any

61   change in water vapor in the UTLS has an exceptionally strong influence on the global

62   radiation budget and thus Earth's climate (Solomon et al., 2010). PyroCbs involve and

63   control cirrus clouds around their tops that reach the UTLS. Changes in cirrus clouds in the

64   UTLS are known to have a strong influence on the global radiation budget (Solomon et al.,

65   2010). The examination of mechanisms through which pyroCbs affect water vapor and

66   cirrus clouds in the UTLS can thus be a way of better understanding climate changes.

67   By definition, pyroCbs initiate over a fire, and the large surface energy release affects

68   their dynamic, thermodynamic and microphysical development. The dynamics of these

69   events has been shown to be mostly controlled by fire-induced latent and sensible heat

70   fluxes at and near the surface. However, questions remain about what role the large

71   concentration of cloud condensation nuclei (CCN) contained in smoke has on the vertical

72   development and microphysical properties. Studies (e.g., Rosenfeld et al., 2008; Storer et

73   al., 2010; Tao et al., 2012) have shown that aerosols affect cumulonimbus clouds, and this

74   raises a possibility that fire-generated aerosols affect pyroCb development. As an example

75   of aerosol impacts on cumulonimbus clouds, these studies have demonstrated that increases

76   in aerosol loading can make the size of droplets (i.e., cloud-liquid particles) smaller.

77   Individual aerosol particles act as seeds for the formation of droplets and thus increasing

78   aerosol loading or increasing aerosol concentrations lead to more droplets formed. More

79   droplets mean more competition among them for available water vapor needed for their

80   condensational growth, and this more competition makes individual droplets smaller.

81   Aerosol-induced smaller sizes of droplets reduce the efficiency of the growth of cloud-

82   liquid particles to raindrops via autoconversion that is a collection process among cloud-

83   liquid particles for them to grow to be raindrops, given that the efficiency is proportional

84   to the sizes. This reduced efficiency leads to less cloud liquid converted to rain. More

85   cloud liquid is thus available for transport to places above the freezing level by updrafts.

86 This eventually induces more freezing of cloud liquid, which enhances parcel buoyancy,

87 and this enhancement invigorates updrafts and associated convection.

88 Compared to the research done on the role played by fire-generated heat fluxes in

89 the development of pyroCbs and their effects on water vapor and cirrus clouds in the UTLS,

90 the research on that role by fire-generated aerosols has been scarce. Motivated by this lack

91 of understanding, this paper focuses on the role by those aerosols in the development of a

92 pyroCb and its effects on water vapor and cirrus clouds in the UTLS. To examine that role,

93 this study extends the previous modeling work that was described in Kablick et al. (2018).

94 That modeling work compared effects of fire-generated heat fluxes on the development of

95 a pyroCb and its impacts on the UTLS water vapor and cirrus clouds to those of fire-

96 generated aerosols. In that comparison, those effects of fire-generated aerosols were shown

97 to be negligible as compared to those effects of heat fluxes. However, aerosol effects on

98 cloud development vary with cloud basic properties such as basic updrafts that are

99 determined by environmental conditions (e.g., Khain et al., 2008; Lee et al., 2008; Tao et

100 al., 2012). Basic updrafts are determined by environmental instability as represented by

101 convective available potential energy (CAPE). Lee et al. (2008) have shown that different

102 clouds with different basic updrafts, which are due to different CAPE, show different

103 sensitivity of cloud microphysical and thermodynamic development to aerosol

104 concentration. Hence, it is hypothesized that aerosol effects on the pyroCb development

105 and its impacts on the UTLS water vapor and cirrus clouds can vary depending on the

106 intensity of the pyroCb basic updrafts.

107 Based on this hypothesis, to examine the potential variation of aerosol effects on the

108 pyroCb development and its impacts on the UTLS water vapor and cirrus clouds with the

109 varying basic updrafts of pyroCbs, numerical simulations are performed. These simulations

110 are for a case of a pyroCb which is identical to that in Kablick et al. (2018), and performed

111 by using a cloud-system resolving model (CSRM) which is able to resolve cloud-scale

112 dynamic, thermodynamic and microphysical processes. By resolving these processes that

113 play a critical role in the development of clouds and their interactions with aerosols, we are

114 able to obtain confident information on aerosol effects on the pyroCb development and its

115 impacts the UTLS water vapor and cirrus clouds, and on associated dynamic,

116 thermodynamic and microphysical mechanisms. The basic modeling methodology in this

117 study is similar to that used by Kablick et al. (2018). However, this study uses a more

118 sophisticated microphysical scheme, i.e., a bin scheme, rather than the two-moment bulk

119 scheme used by Kablick et al. (2018). Note that Kablick et al. (2018) examined aerosol

120 effects on the convective development of a specific pyroCb case study, simulating

121 microphysical conditions, detrained water vapor mixing ratios, and cirrus cloud properties

122 only considering a basic updraft framework. The present study expands upon that work by

123 performing sensitivity simulations in which basic updrafts in the pyroCb are allowed to

124 vary, enabling us to ascertain the dependence of those aerosol effects on basic updrafts.

125 Note that CAPE, which determines basic updrafts in convective clouds, are strongly

126 dependent on surface latent and sensible heat fluxes (e.g., Houze, 1993), and in the case of

127 pyroCb these fluxes are controlled by fire intensity. Hence, these sensitivity simulations in

128 turn enable us to study the dependence of those aerosol effects on fire intensity. Here, we

129 see that the pyroCb basic updrafts are controlled by fire intensity and thus the pyroCb basic

130 updrafts are referred to as fire-driven updrafts, henceforth.

131   Aerosol effects on clouds are initiated by an increase in aerosol concentration, which

132 can be caused by an increase in aerosol emission at and near the surface, and dependent on

133 how much aerosol concentration increases, or on the magnitude of an increase in aerosol

134 concentration, i.e., aerosol perturbation (e.g., Rosenfeld et al., 2008; Koren et al., 2012).

135 This dependence has not been examined in Kablick et al. (2018) and this study examines

136 this dependence by performing additional sensitivity simulations where the magnitude of

137 aerosol perturbation varies.

138

139 **2. CSRM**

140

141 We use the Advanced Research Weather Research and Forecasting (ARW) model, a

142 nonhydrostatic compressible model, as the CSRM. Prognostic microphysical variables are

143 transported with a fifth-order monotonic advection scheme (Wang et al., 2009). Shortwave

144 and longwave radiation parameterizations have been included in all simulations by

145 adopting the Rapid Radiation Transfer Model (RRTM; Mlawer et al., 1997; Fouquart and

146 Bonnel, 1980).

147   To represent the microphysical processes, the CSRM adopts a bin scheme based on

148 the Hebrew University Cloud Model described by Khain et al. (2009). The bin scheme

149 solves a system of kinetic equations for the size distribution functions of water drops, ice

150 crystals (plate, columnar and branch types), snow aggregates, graupel and hail, as well as

151 cloud condensation nuclei (CCN) and ice nuclei (IN). Each size distribution is represented

152 by 33 mass doubling bins, i.e., the mass of a particle m_k in the kth bin is determined as m_k

153 $= 2m_{k-1}$.

154   The cloud-droplet nucleation parameterization, which is based on Köhler theory, is

155 used to represent cloud-droplet nucleation. Arbitrary aerosol mixing states and arbitrary

156 aerosol size distributions can be fed to this parameterization. To represent heterogeneous

157 ice-crystal nucleation, the parameterizations by Lohmann and Diehl (2006) and Möhler et

158 al. (2006) are used. In these parameterizations, contact, immersion, condensation-freezing,

159 and deposition nucleation paths are all considered by taking into account the size

160 distribution of IN. Homogeneous aerosol (or haze particle) and droplet freezing, based on

161 the size distribution of droplets, is also considered following the theory developed by Koop

162 et al. (2000).

163

164 **3. Case description and simulations**

165

166   **3.1 Control run**

167

168 The control run for an observed pyroCb case is performed over a forested site in the

169 Canadian Northwest Territories (60.03° N, 115.45° W). Kablick et al. (2018) give details

170 about the site and the pyroCb case. The control run is identical to the Full Simulation in

171 Kablick et al. (2018) except for the different microphysical schemes between them;

172 remember that this study uses a bin scheme, while Kablick et al. (2018) used a bulk scheme.

173 The control run is performed for one day from 12:00 GMT on August 5th to 12:00 GMT

174 on August 6th in 2014 and captures the initial, mature, and decaying stages of the pyroCb.

175 This simulation is performed in a three dimensional domain with horizontal and vertical

176 lengths of 300 km and 20 km, respectively. For the simulation, the horizontal resolution is

177   500 m and the vertical resolution is 200 m to resolve cloud dynamic, thermodynamic and

178   microphysical processes.

179   Figure 1 shows a satellite image of the observed pyroCb when it is about to advance

180   into its mature stage. In Figure 1, the red circle marks the fire spot whose spatial length is

181   ~ 40 km. To emulate this in the simulation, at the center of the simulation domain, a fire

182   spot with a diameter of 40 km is placed as shown in Figure 2. In the fire spot, the surface

183   latent and sensible heat fluxes are set at 1800 and 15000 W m^{-2}, respectively. In areas

184   outside of the fire spot in the domain, the surface latent and sensible heat fluxes are set at

185   310 and 150 W m^{-2}, respectively. These surface heat-flux values follow the previous

186   studies which are Trentmann et al. (2006) and Luderer et al. (2006) and adopt boreal forest

187   emissions. Following Kablick et al. (2018), the surface heat-flux values are prescribed

188   with no temporal variation and no consideration of interactions between heat fluxes and

189   the atmosphere in the control run. Hence, the setup for the surface heat fluxes is idealized

190   and this enables a better isolation of aerosol effects themselves on the pyroCb development

191   and its impacts on the UTLS water vapor and cirrus clouds for the given surface heat fluxes

192   by excluding effects of interactions between the surface heat fluxes and atmosphere on

193   those development and impacts.

194   For the selected pyroCb case, aerosol properties that can be represented by aerosol

195   chemical composition, size distribution and concentration are unknown. Hence, in the fire

196   spot for the first time step, the concentration of aerosols acting as CCN is prescribed to be

197   15000 cm^{-3} in the planetary boundary layer (PBL), and decreases exponentially with height

198   above the PBL top. Outside of the fire spot for the first time step, the concentration of

199   aerosols acting as CCN is prescribed to be 150 cm^{-3} in the PBL and also decreases

200   exponentially with height above this layer. For the control run, the other aerosol properties

201   are assumed to follow typical values determined in previous studies. For example, Reid et

202   al. (2005) have shown that aerosol mass produced by forest fires is generally composed of

203   ~50-70% of organic-carbon (OC) compounds, ~5-10% of black-carbon (BC) material, and

204   ~20-45% of inorganic species. Based on those results, the approximate median value of

205   each chemical component percentage range is used in the control run. Aerosol particles

206   are assumed to be composed of 60% OC, 8% BC, and 32% inorganic species. In the control

207   run, OC is assumed to be water soluble and composed of (by mass) 18 % levoglucosan

208 (C6H10O5, density = 1600 kg m^{-3}, van't Hoff factor = 1), 41 % succinic acid (C4H6O4,

209 density = 1572 kg m^{-3}, van't Hoff factor = 3), and 41 % fulvic acid (C33H32O19, density

210 = 1500 kg m^{-3}, van't Hoff factor = 5) based on typically observed chemical composition of

211 OC compounds over fire sites (Reid et al., 2005). In the control run, the inorganic species

212 is assumed to be ammonium sulfate, a representative inorganic species associated with fires

213 (Reid et al., 2005). This chemical composition taken for aerosol particles is assumed to be

214 spatiotemporally unvarying in the control run. According to Reid et al. (2005),

215 Knobelspiessel et al. (2011), and Lee et al. (2014), it is reasonable to assume that the initial

216 aerosol size distribution follows the unimodal lognormal distribution in fire sites. Hence,

217 the control run adopts the unimodal lognormal distribution as an initial aerosol size

218 distribution. Those studies have indicated that in general, median aerosol diameter and

219 standard deviation of the distribution range from ~0.01 to ~0.03 μm and from ~2.0 to ~2.2,

220 respectively. By taking the approximate median value of each of these ranges, median

221 aerosol diameter and standard deviation of the adopted unimodal distribution are assumed

222 to be 0.02 μm and 2.1, respectively, for the control run. The unimodal distribution, which

223 is adopted by the simulation, in the PBL over the fire spot is shown in Figure 3 with log-

224 scales for x- and y-axes. For the control run, aerosol properties of IN and CCN are assumed

225 to be identical except that at the first time step, the IN concentration is 100 times lower

226 than the CCN concentration. This is based on a general difference in concentration between

227 CCN and IN (Pruppacher and Klett, 1978).

228   In Figure 1, the observed cirrus cloud at the top of the pyroCb is located to the

229 northeast of the fire spot due to the northeastward winds at the altitude of the cirrus cloud.

230 The cloud first formed around the fire spot. However, winds advected it northeastward.

231 The extent of the observed cirrus cloud is ~100 km. Figure 2 shows the field of cloud-ice

232 mass density at the top of the simulated pyroCb and at a time that corresponds to the

233 satellite image in Figure 1. This field in Figure 2 represents the simulated cirrus cloud in

234 the control run. As observed, the simulated cirrus is located to the northeast of the fire spot

235 and the extent of the simulated cirrus cloud is ~ 100 km. Hence, we see that there is good

236 agreement in the morphology of the cirrus cloud between the observation and the

237 simulation.

238   Figure 4 shows the vertical distribution of the cloud reflectivity field in dBZ, which

239   is observed by the Cloudsat and averaged over the Cloudsat path, and its simulated

240   counterpart in the control run. The details of the reflectivity field are given in Kablick et al.

241   (2018). There is good agreement between observed and simulated cloud reflectivity fields.

242   The agreement in the observed and simulated cirrus cloud and reflectivity fields

243   demonstrates that the pyroCb-case simulation is reasonable.

244

245   **3.2 Low-aerosol run**

246

247   To see the role played by fire-generated aerosols in the development of the pyroCb and its

248   effects on water vapor and cirrus clouds in the UTLS, we repeat the control run by reducing

249   aerosol concentration in the fire spot from 15000 cm^{-3} to the background aerosol

250   concentration (i.e., 150 cm^{-3}). This reduction removes fire-generated aerosols in the fire

251   spot. The only difference is in aerosol concentration in the fire spot and there are no other

252   differences in the simulation setup which is described in Section 3.1 between the control

253   run and this repeated run. Hence, comparisons between the control run and this repeated

254   run, which is referred to as the low-aerosol run, will identify the role played by fire-

255   generated aerosols in the pyroCb development and its impacts on the UTLS water vapor

256   and cirrus clouds. Here, the low-aerosol run is identical to the Low Aerosol Simulation in

257   Kablick et al. (2018) except for the different microphysical schemes between them.

258

259   **3.3 Additional runs**

260

261   We examine the above-mentioned potential variation of effects of fire-generated aerosols

262   on the pyroCb development and its impacts on the UTLS water vapor and cirrus clouds

263   with varying fire intensity and associated fire-driven updrafts. For the examination, we

264   repeat the control run by varying fire intensity. Remember that surface latent and sensible

265   heat fluxes on which fire-driven updrafts in convective clouds are strongly dependent are

266   controlled by fire intensity. Hence, fire intensity can be represented by fire-induced surface

267   latent and sensible heat fluxes and the variation of fire intensity in the repeated control run

268   is accomplished by the variation of these fire-induced surface heat fluxes. As a first step

269   for the examination, the control run is repeated by reducing fire-induced surface latent and

270   sensible heat fluxes by a factor of 2. Then, the control run is repeated again by reducing

271   these fluxes by a factor of 4. The first repeated run represents a case with medium fire

272   intensity, while the second repeated run represents a case with weak fire intensity. Relative

273   to these repeated runs, the control run represents a case with strong fire intensity.

274   Henceforth, the first repeated run is referred to as "the medium run" and the second

275   repeated run is referred to as "the weak run". Then, to see effects of fire-generated aerosols

276   on the pyroCb development and its impacts on the UTLS water vapor and cirrus clouds for

277   each of those cases with different fire intensity, the medium run and the weak run are

278   repeated with the identical initial aerosol concentration to that in the low-aerosol run. The

279   repeated medium run and weak run are referred to as "the medium-low run" and "the weak-

280   low run", respectively. The control run, the medium run, and the weak run are the polluted-

281   scenario runs, while the low-aerosol run, the medium-low run, and the weak-low run are

282   the clean-scenario runs. Comparisons between the medium run and the medium-low run

283   and those between the weak run and the weak-low run isolate those effects of fire-generated

284   aerosols for the case of medium fire intensity and the case of weak fire intensity,

285   respectively. Comparisons between the control run and the low-aerosol run identify those

286   aerosol effects for the case of strong fire intensity.

287   Effects of fire-generated aerosols on the pyroCb development and its impacts on the

288   UTLS water vapor and cirrus clouds can also be dependent on how large fire-induced

289   increases in aerosol concentrations are or the magnitude of fire-induced aerosol

290   perturbation in a fire spot. Motivated by this, the previously described simulations are

291   repeated by varying the magnitude of aerosol perturbation in the fire spot. To test the

292   sensitivity of results to the magnitude of fire-induced aerosol perturbation, for each fire

293   intensity, we repeat the polluted-scenario run by increasing and reducing the magnitude by

294   a factor of 2 in the fire spot but not outside of the fire spot. These simulations with the

295   increased magnitude have an aerosol concentration of $30000\ cm^{-3}$ at the first time step over

296   the fire spot in the PBL and are referred to as the control-30000 run, the medium-30000

297   run, and the weak-30000 run for strong, medium, and weak fire intensity, respectively.

298   These simulations with the reduced magnitude have an aerosol concentration of   7500

299   cm^{-3} at the first time step over the fire spot in the PBL and are referred to as the control-

300   7500 run, the medium-7500 run, and the weak-7500 run for strong, medium, and weak fire

301   intensity, respectively. Motivated by the analysis described in Section 4.2, we additionally

302   repeat the medium run and the weak run with aerosol concentrations of   2000 and 1000

303   cm^{-3} at the first time step over the fire spot in the PBL, respectively. The repeated medium

304   (weak) run is referred to as the medium-2000 (the weak-1000) run. Table 1 summarizes

305   the simulations.

306

4. Results

308

309   Results from the control run and the low-aerosol run, which are equivalent to the Full

310   Simulation and the Low Aerosol Simulation in Kablick et al. (2018), respectively, are

311   described here. Kablick et al. (2018) mainly focused on comparisons themselves between

312   aerosol effects and heat-flux effects on pyroCb development and its impacts on the UTLS

313   water vapor and cirrus clouds. In this study, we expand upon the results of Kablick et al.

314   (2018) by providing additional details of the simulation results by focusing on the impacts

315   of pyroCb development on the UTLS water vapor and cirrus clouds, and aerosol effects on

316   pyroCb development.

317   Figure 5 shows the vertical distributions of the averaged updraft mass fluxes over

318   cloudy areas, i.e., areas where the sum of liquid-water content (LWC) and ice-water content

319   (IWC) is non-zero, and over the simulation period between 17:00 GMT on August 5th and

320   12:00 GMT on August 6th in the control run and the low-aerosol run for the case of strong

321   fire intensity. 17:00 GMT on August 5th is a time around which the pyroCb starts to from

322   and 12:00 GMT on August 6th is the end of the simulation period. In this study, drops with

323   radii smaller (greater) than 20 µm are classified as droplets (raindrops). For the calculation

324   of LWC (IWC), we only considered droplets (ice crystals). Stated differently, droplet mass

325   but not rain mass is used to obtain LWC and the mass of ice crystals but not the mass of

326   snow aggregates, graupel and hail is used to obtain IWC.

327   The updraft mass flux is one of the most representative variables that are indicative

328   of the cloud dynamic intensity and the magnitude of convective invigoration. As seen in

329   Figure 5, the control run and the low-aerosol run for strong fire intensity have similar

330   updraft mass fluxes. Table 2 gives the averaged values of updraft mass fluxes over cloudy

Atmospheric
Chemistry
and Physics
Discussions

Open Access

EGU

331   areas at all altitudes and over the simulation period between 17:00 GMT on August 5th and

332   12:00 GMT on August 6th for simulations. In Figure 5 and Table 2, updraft mass fluxes in

333   the control run are only ~3% greater than those in the low-aerosol run. Given the

334   hundredfold difference in aerosol loading over the fire spot between the runs, this 3%

335   difference in updraft fluxes is negligibly small.

336   Water vapor around and above the tropopause or the UTLS plays an important role in

337   the global radiation budget, thus garnering much attention from the climate-change

338   community. Motivated by this, we examine the role played by the pyroCb in the UTLS

339   water vapor. The vertical distributions of averaged water-vapor mass density around and

340   above the tropopause (~ 13 km) are shown in Figure 6. The water-vapor mass density

341   shown by colored lines in Figure 6 is averaged over cloudy grid columns that have the non-

342   zero sum of liquid-water path (LWP) and ice-water path (IWP) and over the simulation

343   period between 17:00 GMT on August 5th and 12:00 GMT on August 6th. For the

344   calculation of LWP (IWP), we only considered droplets (ice crystals) as for the calculation

345   of LWC (IWC). The black line in Figure 6 shows the average of water-vapor mass density

346   over non-cloudy grid columns that have the zero sum of LWP and IWP and over the

347   simulation period between 17:00 GMT on August 5th and 12:00 GMT on August 6th in the

348   control run. This represents the background water-vapor mass density. Table 2 shows the

349   averaged values of water-vapor mass density over altitudes between 13 and 16 km for

350   simulations.

351   As seen in Figure 6, 16 km is an altitude to which the non-zero water-vapor mass

352   density over cloudy columns extends. The comparison between water-vapor mass density

353   over the cloudy columns and that over non-cloudy columns in the control run as shown in

354   Figure 6 and Table 2 demonstrates that there is a substantial increase in the amount of water

355   vapor in the UTLS due to the pyroCb. There is about five times greater water-vapor mass

356   over the cloudy columns that represent the pyroCb area than in the background outside the

357   pyroCb area in the control run.

358   Updrafts in the pyroCb transport water vapor to the UTLS, which leads to the

359   substantial increase in the amount of water vapor in the UTLS over the pyroCb area. For

360   the simulation period between 17:00 GMT on August 5th and 12:00 GMT on August 6th,

361   the averaged water-vapor mass fluxes at the tropopause over cloudy and non-cloudy grid

362   columns are 8.30×10^{-6} and 0.57×10^{-6} kg m^{-2} s^{-1}, respectively. Due to the presence of the

363   pyroCb and associated updrafts in cloudy grid columns, there are substantial increases in

364   water vapor fluxes at the tropopause over those cloudy grid columns as compared to those

365   fluxes in the background over non-cloudy grid columns. This leads to larger water vapor

366   mass in the UTLS over the pyroCb than in the background outside the pyroCb or the

367   pyroCb area in the control run. It is also shown that the vertical extent of water vapor is

368   extended further up to ~ 16 km by the pyroCb as compared to the extent of ~14 km in the

369   background (Figure 6).

370   Similar to the situation with updraft mass fluxes, there is only a small (~2%) increase

371   in the averaged water vapor mass in the UTLS, as shown in Figure 6 and Table 2, in the

372   control run as compared to that in the low-aerosol run for strong fire intensity. This small

373   variation in updraft mass fluxes between the control run and the low-aerosol run also results

374   in a small variation in the transportation of water vapor to the UTLS and the averaged

375   water-vapor fluxes at the tropopause between these two simulations. These averaged

376   fluxes are over cloudy columns for the simulation period between 17:00 GMT on August

377   5th and 12:00 GMT on August 6th. The averaged water-vapor fluxes vary from 8.30×10^{-6}

378   kg m^{-2} s^{-1} in the control run to 8.21×10^{-6} kg m^{-2} s^{-1} in the low-aerosol run.

379   In addition to water vapor in the UTLS, cloud ice or ice crystals around the tropopause

380   play an important role in the global radiation budget. These ice crystals comprise cirrus

381   clouds. To identify the role played by the pyroCb in cirrus clouds, Figure 7 shows the

382   averaged cloud-ice mass density over cloudy areas for the simulation period of 17:00 GMT

383   on August 5th to 12:00 GMT on August 6th in the simulations. The altitude of homogeneous

384   freezing is at ~ 9 km , so cirrus clouds which are composed of ice crystals only are between

385   ~ 9 km and ~13 km. Between ~ 9 km and ~ 13 km, the averaged cloud-ice mass density in

386   the control run is shown in Figure 7, and ranges from ~ 0.028 to ~ 0.037 g m^{-3}. In non-

387   cloudy areas and in the clear sky background outside the pyroCb, cloud-ice mass density

388   equals zero. Hence in the control run, the pyroCb increases cloud-ice mass density between

389   ~0.028 to ~0.037 g m^{-3} over the background.

390   Updrafts in the pyroCb produce supersaturation, which leads to the generation of cloud-

391   ice mass and associated cirrus clouds via deposition, the primary source of cloud-ice mass.

392   Similar to the situation with updraft mass fluxes, comparisons between the control run and

393   the low-aerosol run for strong fire intensity show that there is only a small increase (~4%)

394   in cloud-ice mass in the control run particularly between 9 km and 13 km, as shown in

395   Figure 7 and Table 2, as compared to that in the low-aerosol run. Due to the negligible

396   variation of updraft mass fluxes, there are negligible variations of supersaturation and

397   deposition between the simulations as seen in Figure 8, and thus a negligible variation of

398   cloud-ice mass between the control run and the low-aerosol run. Figure 8 shows the vertical

399   distributions of the averaged deposition rate over cloudy areas for the simulation period of

400   17:00 GMT on August 5th to 12:00 GMT on August 6th.

401   In summary, the pyroCb and associated updrafts cause a substantial enhancement of

402   the transportation of water vapor to the UTLS. They also produce cirrus clouds. The role,

403   which is played by fire-generated aerosols and their effects on the pyroCb and its updrafts,

404   in the enhancement of the transportation of water vapor to the UTLS and in the production

405   of cirrus cloud is not significant for strong fire intensity.

406

407   **4.1 Dependence of aerosol effects on fire intensity**

408

409   The weak sensitivity of updrafts, water vapor, and cirrus clouds to aerosol loading in the

410   pyroCb may be related to fire intensity. When fire-generated surface heat fluxes and fire

411   intensity are increased, it is likely that in-cloud latent heat is also increased because a major

412   source of in-cloud latent heating is surface heat flux. Therefore, the aerosol-induced

413   perturbations of latent heating may be relatively small compared with large in-cloud latent

414   heat contributed by surface fluxes with very intense burning. In other words, aerosol-

415   induced increases in parcel buoyancy and updrafts are relatively small compared with the

416   large buoyancy and strong fire-driven updrafts produced by strong fire intensity and the

417   associated large in-cloud latent heat.

418   Considering that a major source of in-cloud latent heat is surface heat fluxes, when the

419   fire-generated surface heat fluxes and the fire intensity are reduced, in-cloud latent heat is

420   also likely to be smaller. Here, we are interested in how the magnitude of an aerosol-

421   induced perturbation of latent heating for a pyroCb with weak fire intensity is compared to

422   that with strong fire intensity. This is just based on a possibility that with background in-

Atmospheric
Chemistry
and Physics
Discussions

15

423 cloud latent heat varying with fire intensity, the relative magnitude of aerosol-induced

424 perturbation of latent heat to surface flux-dominated latent heat may vary.

425

426 **4.1.1 Updrafts and the UTLS water vapor and cirrus cloud**

427

428 Figure 9 shows the averaged updraft mass fluxes over cloudy areas at each altitude in the

429 runs with different fire intensity for the simulation period of 17:00 GMT on August 5th to

430 12:00 GMT on August 6th. Here, the averaged updraft mass fluxes in the low-aerosol run,

431 the medium-low run and the weak-low run represent fire-driven updrafts for strong,

432 medium and weak fire intensity, respectively. Due to different fire intensity and associated

433 CAPE, fire-driven updrafts vary between these runs. The variation of these fluxes between

434 the low-aerosol run and the control run for strong fire intensity, between the medium-low

435 run and the medium run for medium fire intensity, and between the weak-low run and the

436 weak run for weak fire intensity, respectively, is induced by fire-generated aerosols. As

437 seen in Figure 9 and Table 2, all of the cases of weak, medium and strong fire intensity

438 show aerosol-induced increases in updraft mass fluxes. Of interest is that the percentage

439 increase in updrafts in the case of weak fire from those in the weak-low run to those in the

440 weak run is the greatest, while the percentage increase in the case of strong fire from

441 updrafts in the low-aerosol run to those in the control run is the smallest. The percentage

442 increase for the case of medium fire from updrafts in the medium-low run to those in the

443 medium run is intermediate (Figure 9 and Table 2). Here, the percentage difference,

444 including both the percentage increase and decrease, is the relative difference in the value

445 of variables between the control run and the low-aerosol run for strong fire intensity,

446 between the medium run and the medium-low run for medium fire intensity or between the

447 weak run and the weak-low run for weak fire intensity. This percentage difference for

448 strong fire intensity is obtained as follows in this study:

449

450 $$\frac{The\ control\ run\ minus\ the\ low-aerosol\ run}{The\ low-aerosol\ run} \times 100\ (\%) \qquad (1)$$

451

452 The percentage difference for medium fire intensity is obtained by replacing the control

453 run with the medium run and replacing the low-aerosol run with the medium-low run in

454   Equation (1). The percentage difference for weak fire intensity is obtained by replacing the

455   control run with the weak run and replacing the low-aerosol run with the weak-low run in

456   Equation (1). Associated with those greatest increases in updraft mass fluxes, the

457   percentage increases in water vapor and cloud-ice mass in the UTLS, which are calculated

458   by Equation (1), are the greatest in the case of weak fire as seen in Figures 10 and 11 and

459   Table 2. Figures 10 and 11 show the averaged water-vapor and cloud-ice mass density at

460   each altitude, respectively, over cloudy areas for the simulation period of 17:00 GMT on

461   August 5th to 12:00 GMT on August 6th in the runs with different fire intensity. Associated

462   with those smallest increases in updraft mass fluxes, the percentage increases in water

463   vapor and cloud-ice mass in the UTLS are the smallest in the case of strong fire as seen in

464   Figures 10 and 11 and Table 2. Associated with the medium increase in updraft mass fluxes,

465   the percentage increases in water vapor and cloud-ice mass in the UTLS are intermediary

466   in the case of medium fire as compared to the cases of strong and weak fire (Figures 10

467   and 11 and Table 2).

468

469   **4.1.2 Volume mean radius of droplets (R_v)**

470

471   **a.   Cloud droplet number concentration (CDNC) and LWC**

472

473   The simulation period is divided into four sub-periods for this next analysis: period 1

474   between 17:00 and 19:00 GMT on August 5th, period 2 between 19:00 and 21:00 GMT on

475   August 5th, period 3 between 21:00 GMT and 23:00 GMT on August 5th, and period 4

476   between 23:00 GMT on August 5th and 12:00 GMT on August 6th. The initial formation of

477   the pyroCb corresponds with the beginning of period 1, and along with periods 2 and 3

478   correspond to the initial stages of cloud development, while period 4 corresponds to the

479   mature and the decaying stages. As seen in Figure 12, CDNC, which is averaged over

480   cloudy areas at all altitudes and over period 1, decreases as the fire intensity and updrafts

481   decrease. However, the control run, the medium run, and the weak run have the much

482   higher averaged CDNC than the low-aerosol run, the medium-low run, and the weak-low

483   run, respectively. Remember that the control run, the medium run and the weak run have

484   higher aerosol concentrations than the low-aerosol run, the medium-low run and the weak-

485   low run, respectively, over the fire spot (Table 1). Increasing CDNC enhances competition

486   among droplets for a given amount of water, which is available for the condensational

487   growth of droplets, in a cloud. Enhanced competition eventually curbs the condensational

488   growth and reduces droplet size, which is represented by R_v in this study. This explains

489   why R_v, which is averaged over cloudy areas at all altitudes and over period 1, is smaller

490   in the control run than in the low-aerosol run for strong fire intensity, in the medium run

491   than in the medium-low run for medium fire intensity, and in the weak run than in the

492   weak-low run for weak fire intensity, respectively, as seen in Figure 12. Of interest is that

493   as fire intensity weakens, although the averaged CDNC reduces, which tends to lower the

494   competition among droplets, the averaged R_v decreases not only among the control run, the

495   medium run and the weak run with higher aerosol concentrations over the fire spot but also

496   among the low-aerosol run, the medium-low run and the weak-low run with lower aerosol

497   concentrations over the fire spot as shown in Figure 12. This is because R_v is proportional

498   to $(\frac{LWC}{CDNC})^{\frac{1}{3}}$. Here, LWC represents the given amount of water which is available for the

499   condensational growth of droplets. This proportionality means that for a given CDNC, a

500   decrease in LWC also causes R_v to decrease, i. e., a decrease in the available amount of

501   water for the condensational growth with no changes in CDNC induces a decrease in R_v.

502   As shown in Figure 12, LWC, which is averaged over cloudy areas at all altitudes and over

503   period 1, also decreases with weakening fire intensity and updrafts not only among the

504   control run, the medium run and the weak run but also among the low-aerosol run, the

505   medium-low run and the weak-low run. Effects of LWC on R_v, which weakens as fire

506   intensity weakens, outweigh those of CDNC and this leads to the decrease in the averaged

507   R_v with weakening fire intensity as seen in Figure 12.

508   Note that the averaged LWC in the control run is similar to that in the low-aerosol run

509   for strong fire intensity, while the averaged LWC in the medium run is similar to that in

510   the medium-low run for medium fire intensity. The averaged LWC in the weak run is also

511   similar to that in the weak-low run for weak fire intensity. The averaged LWC reduces with

512   weakening fire intensity from that in the control run to that in the weak run through that in

513   the medium run during period 1 (Figure 12). This reduction is similar to the reduction in

514   the averaged LWC from that in the low-aerosol run to that in the weak-low run through

515   that in the medium-low run during period 1 (Figure 12). Considering this, the fact that the

516 averaged CDNC is much higher in the control run than in the low-aerosol run leads to a

517 situation where $(\frac{LWC}{CDNC})$, which is the base of $(\frac{LWC}{CDNC})^{\frac{1}{3}}$, and thus R_v are much smaller in the

518 control run than in the low-aerosol run for strong fire intensity; the fact that the averaged

519 CDNC is much higher in the medium run than in the medium-low run leads to a situation

520 where $(\frac{LWC}{CDNC})$ and R_v are much smaller in the medium run than in the medium-low run for

521 medium fire intensity; the fact that the averaged CDNC is much higher in the weak run

522 than in the weak-low run leads to a situation where $(\frac{LWC}{CDNC})$ and R_v are much smaller in the

523 weak run than in the weak-low run for weak fire intensity.

524 Using the averaged LWC and the averaged CDNC that are shown in Figure 12,

525 $\left(\frac{LWC}{CDNC}\right)$ is calculated. $(\frac{LWC}{CDNC})$ reduces from 4.27×10^{-14} kg in the control run for strong fire

526 intensity to 8.08×10^{-15} kg in the weak run for weak fire intensity through 3.09×10^{-14} kg in

527 the medium run for medium fire intensity. $(\frac{LWC}{CDNC})$ reduces from 1.1×10^{-12} kg in the low-

528 aerosol run for strong fire intensity to 8.1×10^{-13} kg in the weak-low run for weak fire

529 intensity through 1.00×10^{-12} kg in the medium-low run for medium fire intensity. Here, the

530 absolute variation of $(\frac{LWC}{CDNC})$ with varying fire intensity is about one order of magnitude

531 smaller among the control run, the medium run and the weak run than among the low-

532 aerosol run, the medium-low run and the weak-low run during period 1. Despite this, the

533 absolute and percentage variations of $(\frac{LWC}{CDNC})^{\frac{1}{3}}$ and thus the averaged R_v is greater among

534 the control run, the medium run and the weak run than among the low-aerosol run, the

535 medium-low run and the weak-low run during period 1. This is due to the characteristics

536 of a function of the form " $x^{\frac{1}{3}}$ " whose reduction with reducing x is greater when x is

537 positive and smaller for an identical decrement in x. $(\frac{LWC}{CDNC})^{\frac{1}{3}}$ varies by 1.50×10^{-5} kg from

538 3.50×10^{-5} kg in the control run for strong fire intensity to 2.00×10^{-5} kg in the weak run for

539 weak fire intensity, while it varies by 9.80×10^{-6} kg from 1.03×10^{-4} kg in the low-aerosol

540 run for strong fire intensity to 9.32×10^{-5} kg in the weak-low run for weak fire intensity.

541 Associated with this, the averaged R_v, as seen in Figure 12, shows a 47 % reduction from

542 3.20 μm in the control run for strong fire intensity to 1.70 μm in the weak run for weak

Atmospheric
Chemistry
and Physics
Discussions

543   intensity, and the averaged R_v shows a 10 % reduction from 7.75 μm in the low-aerosol

544   run for strong intensity to 6.98 μm in the weak-low run for weak intensity during period 1.

545   Figure 13 plots the function $y = x^{\frac{1}{3}}$ to demonstrate the behavior of R_v (y) with respect

546   to $\frac{LWC}{CDNC}$ (x). In Figure 13 the arbitrary values x_{L1} and x_{L2} are large, and x_{S1} and x_{S2} are small.

547   In Figure 13, a situation is assumed where the variation of x-value from x_{L1} to x_{L2} is greater

548   than that from x_{S1} and x_{S2}. The variation between x_{S1} and x_{S2} emulates the variation of

549    $(\frac{LWC}{CDNC})$ among the control run, the medium run and the weak run with higher aerosol

550   concentrations over the fire spot, while the variation between x_{L1} and x_{L2} emulates the

551   variation of $(\frac{LWC}{CDNC})$ among the low-aerosol run, the medium-low run and the weak-low

552   run with lower aerosol concentrations over the fire spot. Here, x and y correspond to $(\frac{LWC}{CDNC})$

553   and $(\frac{LWC}{CDNC})^{\frac{1}{3}}$, respectively. Despite the smaller variation between x_{S1} and x_{S2} than that

554   between x_{L1} and x_{L2}, the corresponding variation of y is greater between x_{S1} and x_{S2} than

555   between x_{L1} and x_{L2}. This graphically explains the larger variation of $(\frac{LWC}{CDNC})^{\frac{1}{3}}$ and thus the

556   averaged R_v in Figure 12 despite the smaller variation of $(\frac{LWC}{CDNC})$ among the control run, the

557   medium run and the weak run than among the low-aerosol run, the medium-low run and

558   the weak-low run.

559

560   **b. Equilibrium supersaturation**

561

562   During period 1 between 17:00 and 19:00 GMT on August 5th, the lower value of the

563   equilibrium supersaturation in rising air parcels in the control run than in the low-aerosol

564   run for strong fire intensity, in the medium run than in the medium-low run for medium

565   fire intensity, and in the weak run than in the weak-low run for weak fire intensity,

566   respectively, aids the greater reduction in R_v among the control run, the medium run and

567   the weak run than among the low-aerosol run, the medium-low run and the weak-low run

568   with weakening fire intensity as seen in Figure 12. Remember that the control run, the

569   medium run and the weak run have higher aerosol concentrations than the low-aerosol run,

570   the medium-low run and the weak-low run, respectively, over the fire spot (Table 1). Lee

571 et al. (2009) and Lee and Penner (2010) have also shown the lower equilibrium

572 supersaturation in simulations with higher aerosol concentrations than simulations with

573 lower aerosol concentrations. The rate of parcel supersaturation change is expressed by the

574 following equation as shown in Khain et al. (2000):

575

576 $\frac{dS}{dt} = A_1 W - A_2 \frac{dq_L}{dt}$ (2)

577

578 In Equation (2), S is parcel supersaturation, while W and q_L are the updraft speed and the

579 mixing ratio of cloud-liquid particles (or droplets) in a rising air parcel, respectively. The

580 coefficients A_1 and A_2 are functions of thermodynamic parameters such as temperature,

581 latent heat of vaporization, air viscosity and pressure. The first term in Equation (2)

582 represents the generation of supersaturation by adiabatic air cooling, while the second term

583 represents the depletion of supersaturation by the consumption of water vapor via the

584 condensational growth of unactivated aerosol particles. At first, supersaturation in a rising

585 air parcel increases with time as the parcel rises from around the surface. However,

586 eventually, as the parcel goes up further, the increasing trend of supersaturation stops and

587 its decreasing trend starts in the rising air parcel, which is when $\frac{dS}{dt}$ becomes zero and

588 supersaturation reaches its maximum value or becomes equilibrium supersaturation

589 (Rogers and Yau, 1991). Rogers and Yau (1991) have shown that a higher aerosol

590 concentration and associated higher consumption of water vapor by aerosol particles before

591 supersaturation reaches its equilibrium value induce lower equilibrium supersaturation for

592 a given set of updraft speed, aerosol composition, a form of aerosol size distribution and

593 thermodynamic condition in a rising air parcel by using an idealized conceptual model.

594 This is consistent with Lee et al. (2009) and Lee and Penner (2010) who used a large-eddy

595 simulation model for a real case. Rogers and Yau (1991) have also shown that a lower

596 updraft speed and associated less adiabatic cooling induce lower equilibrium

597 supersaturation for a given set of aerosol concentration, aerosol composition and a form of

598 aerosol size distribution. According to well-known Köhler theory, smaller aerosol particles

599 have greater critical supersaturation for a given aerosol chemical composition and aerosol

600 particles with critical supersaturation, which is lower than the equilibrium supersaturation,

21

601 are activated (Rogers and Yau, 1991). Hence, as equilibrium supersaturation lowers in a

602 rising air parcel, the minimum size of activated aerosol particles increases for a given

603 aerosol composition as shown in Rogers and Yau (1991). Among aerosol particles that are

604 activated in the rising air parcel, aerosol particles with the minimum size have the largest

605 critical supersaturation, hence, all the particles with larger sizes than the minimum size are

606 activated.

607   During period 1, as fire intensity weakens and updraft speed decreases for the identical

608 initial aerosol concentration, the identical aerosol composition, and the identical assumed

609 form of initial aerosol size distribution, parcel equilibrium supersaturation lowers not only

610 among the low-aerosol run for strong fire intensity, the medium-low run for medium fire

611 intensity and the weak-low run for weak fire intensity but also among the control run for

612 strong fire intensity, the medium run for medium fire intensity and the weak run for weak

613 fire intensity. Also, during period 1, percentage differences in updraft speed, which is

614 averaged over areas with positive updraft speed and period 1, between the control run and

615 the low-aerosol run for strong fire intensity, between the medium run and the medium-low

616 run for medium fire intensity, and between the weak run and the weak-low run for weak

617 fire intensity, respectively, are less than 2% and thus negligibly small. These percentage

618 differences are calculated by Equation (1). During period 1, differences, which is also

619 calculated by Equation (1), in thermodynamic parameters (i.e., temperature, latent heat of

620 vaporization, air viscosity and pressure), which are also averaged over areas with positive

621 updraft speed and period 1, between the control run and the low-aerosol run, between the

622 medium run and the medium-low run, and between the weak run and the weak-low run,

623 respectively, are less than 5% and thus considered negligibly small. However, there are

624 two orders of magnitude higher aerosol concentration over the fire spot in the control run

625 than in the low-aerosol run for strong fire intensity, in the medium run than in the medium-

626 low run for medium fire intensity, and in the weak run than the weak-low run for weak fire

627 intensity, respectively, at the first time step. This is with the identical aerosol composition

628 and the identical assumed form of initial aerosol size distribution between the control run

629 and the low-aerosol run, between the medium run and the medium-low run, and between

630 the weak run and the weak-low run, respectively. Hence, mostly due to differences in

631 aerosol concentration between the control run and the low-aerosol run, between the

632   medium run and the medium-low run, and between the weak run and the weak-low run,

633   respectively, the averaged equilibrium supersaturation and the averaged associated

634   minimum size of activated aerosol particles over areas with positive updraft speed and

635   period 1, are lower and higher, respectively, in the control run than in the low-aerosol run

636   for strong fire intensity, in the medium run than in the medium-low run for medium fire

637   intensity, and in the weak run than the weak-low run for weak fire intensity. Associated

638   with this, as diagrammatically depicted in Figure 14, the increase in the averaged minimum

639   size with weakening fire intensity and associated decreasing updraft speed and equilibrium

640   supersaturation occurs in the size range that is closer to the right tail of the assumed

641   unimodal aerosol size distribution among the control run, the medium run and the weak

642   run than among the low-aerosol run, the medium-low run and the weak-low run. Figure

643   14 is the same as Figure 3 but with linear scales for x- and y-axes. In Figure 14, D_{cs} and

644   D_{cw} represent the averaged minimum size in the low-aerosol run for strong fire intensity

645   and in the weak-low run for weak fire intensity, respectively, while D_{ps} and D_{pw} represent

646   the averaged minimum size in the control run for strong fire intensity and in the weak run

647   for weak fire intensity, respectively. The averaged equilibrium supersaturation reduces

648   from 0.21% in the control run for strong fire intensity to 0.10% in the weak run for weak

649   fire intensity. Associated with this, the averaged minimum size in diameter increases from

650   0.09 μm in the control run for strong fire intensity to 0.12 μm in the weak run for weak fire

651   intensity over period 1. The averaged equilibrium supersaturation reduces from 0.55% in

652   the low-aerosol run for strong fire intensity to 0.31% in the weak-low run for weak fire

653   intensity. Associated with this, the averaged minimum size increases from 0.04 μm in the

654   low-aerosol run for strong fire intensity to 0.07 μm in the weak-low run for weak fire

655   intensity over period 1.

656   The aerosol distribution as depicted in Figure 14 represents the averaged form of the

657   distribution over the simulation domain and period. This indicates that on average, the

658   overall initial form of aerosol size distribution is well maintained over the domain and

659   period, although aerosol concentration in each size bin of the distribution evolves with time

660   and space. The above-described size range, which is associated with the increase in the

661   averaged minimum size with weakening fire intensity and decreasing updraft speed, is

662   between the averaged minimum size with strong fire intensity and that with weak fire

663   intensity as seen in Figure 14. The concentration of aerosol particles with a size, which is

664   closer to the right tail, is lower than that with another size, which is less close to the right

665   tail, as long as these sizes are on the right-hand side of the distribution peak as seen in

666   Figures 3 and 14; since most of aerosol activation occurs for aerosol sizes on the right-hand

667   side of the peak, here we are only concerned with the size ranges on the right-hand side.

668   Stated differently, a larger portion of total aerosol concentration is over a size range that is

669   farther from the right tail than over the other range which is closer to the right tail, in case

670   the size increment over the two ranges is similar as can be seen in Figure 14. Note that

671   associated with similar updraft speeds between the control run and the low-aerosol run for

672   strong fire intensity, between the medium run and the medium-low run for medium fire

673   intensity, and between the weak run and the weak-low run for weak fire intensity,

674   respectively, during period 1, the reduction in updraft speed with weakening fire intensity

675   among the low-aerosol run, the medium-low run and the weak-low run is also similar to

676   that among the control run, the medium run and the weak run during period 1. This

677   contributes to a situation where the increment in the averaged minimum size, which is 0.03

678   micron, among the low-aerosol run, the medium-low run and the weak-low run is similar

679   to that among the control run, the medium run and the weak run during period 1 as

680   diagrammatically depicted in Figure 14. The increment is the averaged minimum size with

681   weak fire intensity minus that with strong fire intensity.

682   All aerosol particles with size greater than the minimum-activation size contribute to

683   the overall CDNC. Accordingly, as seen in Figure 14, the increase in the averaged

684   minimum size as fire intensity weakens reduces the number of aerosol particles that can be

685   activated and droplets. This reduction in the number of activated aerosol particles is equal

686   to the number of aerosol particles in the size range between the averaged minimum size

687   with strong and weak fire intensity. Figure 14 demonstrates that this increase in the

688   minimum-activation size with weakening fire intensity occurs closer to the tail among the

689   control run, the medium run and the weak run than among the low-aerosol run, the medium-

690   low run and the weak-low run. Recall that a large portion of the total aerosol concentration

691   is in the size range which is closer to the right tail of the assumed unimodal aerosol size

692   distribution than that which is less close to the right tail as long as changes in the minimum

693   size in these two size ranges are similar and these ranges are on the right-hand side of the

Atmospheric
Chemistry
and Physics
Discussions

694   aerosol distribution. So, a similar increase in the averaged minimum-activation size for a

695   weakened fire results in a smaller percentage reduction in the total activated aerosol

696   concentration among the control run, the medium run and the weak run than among the

697   low-aerosol run, the medium-low run and the weak-low run during period 1. As seen in

698   Figure 12, CDNC, which is averaged over cloudy areas and period 1, varies by 8% from

699   850 cm^{-3} in the control run with strong fire intensity to 780 cm^{-3} in the weak run with weak

700   fire intensity. The averaged CDNC varies by 76% from 33 cm^{-3} in the low-aerosol run with

701   strong fire intensity to 8 cm^{-3} in the weak-low run with weak fire intensity. This contributes

702   to greater reduction in $(\frac{LWC}{CDNC})^{\frac{1}{3}}$ and thus R$_v$ as fire intensity weakens among the control run,

703   the medium run and the weak run than among the low-aerosol run, the medium-low run

704   and the weak-low run during period 1. This is for a similar LWC between the control run

705   and the low-aerosol run for strong fire intensity, between the medium run and the medium-

706   low run for medium fire intensity, and between the weak run and the weak-low run for

707   weak fire intensity, respectively.

708   The contribution is easily understood if we assume a situation where CDNC and

709   LWC in the control run, the low-aerosol run, the medium run, the medium-low run, the

710   weak run and the weak-low run are identical to those in Figure 12 except for the fact that

711   CDNC reduces by 82% from 850 cm^{-3} in the control run with strong fire intensity to 150

712   cm^{-3} in the weak run with weak fire intensity. In this situation, the CDNC percentage

713   reduction is greater between the control run and the weak run than between the low-aerosol

714   run and the weak-low run with weakening fire intensity. This causes a greater reduction in

715    $(\frac{LWC}{CDNC})^{\frac{1}{3}}$ (and thus R$_v$) between the low-aerosol run and the weak-low run than between the

716   control run and the weak run with weakening fire intensity. $(\frac{LWC}{CDNC})^{\frac{1}{3}}$ varies by 9.80×10^{-6} kg

717   from 1.03×10^{-4} kg in the low-aerosol run for strong fire intensity to 9.32×10^{-5} kg in the

718   weak-low run for weak fire intensity, and it varies by 3.00×10^{-7} kg from 3.50×10^{-5} kg in

719   the control run for strong fire intensity to 3.47×10^{-5} kg in the weak run for weak fire

720   intensity. Hence, the smaller percentage variation of CDNC plays a role in the greater

721   reduction in $(\frac{LWC}{CDNC})^{\frac{1}{3}}$ and thus R$_v$ with weakening fire intensity among the control run, the

722   medium run and the weak run than among the low-aerosol run, the medium-low run and

723   the weak-low run during period 1. Remember that the control run, the medium run and the

724   weak run constitute the polluted-scenario runs with higher aerosol concentrations over the

725   fire spot, and the low-aerosol run, the medium-low run and the weak-low run constitute the

726   clean-scenario runs with lower aerosol concentrations over the fire spot. This larger

727   reduction in R_v for the polluted-scenario case compared with the clean-scenario case—both

728   with similar LWC and LWC reduction—is also reported in Reid et al. (1999). However,

729   Reid et al. (1999) did not explain the cause of the greater R_v reduction for the polluted case.

730   The polluted case has 100 times higher aerosol concentration than the clean case in Reid

731   et al. (1999), which is similar to the polluted-scenario runs as compared to the clean-

732   scenario runs in this study.

733

734   **4.1.3 Autoconversion, freezing, deposition and condensation**

735

736   According to previous studies (e.g., Khairoutdinov and Kogan, 2000; Liu and Daum, 2004;

737   Lee and Baik, 2017), autoconversion is strongly dependent on the size of cloud droplets

738   and is proportional to the size of cloud droplets. This is explained by the fact that the

739   efficiency of collection among droplets is proportional to droplet size (Pruppacher and

740   Klett, 1978; Rogers and Yau, 1991). Larger droplets collect or coalesce with other droplets

741   more efficiently. Autoconversion is a collection process among droplets to form raindrops,

742   which means autoconversion rate and cloud droplet size is proportional. Due to the larger

743   R_v during period 1, the subsequent autoconversion rates, which are averaged over cloudy

744   areas and over period 2, are higher in the low-aerosol run than in the control run for strong

745   fire intensity, in the medium-low run than in the medium run for medium fire intensity, and

746   in the weak-low run than in the weak run for weak fire intensity, respectively (Figure 15a).

747   Due to the larger absolute and percentage reduction in R_v, as described in Section 4.1.2,

748   there is a larger absolute and percentage reduction in autoconversion rate among the control

749   run, the medium run and the weak run than among the low-aerosol run, the medium-low

750   run and the weak-low run with weakening fire intensity during period 2 (Figure 15a). The

751   averaged autoconversion rates over period 2 reduce from 3.61×10^{-6} g m^{-3} s^{-1} in the control

752   run with strong fire intensity to 0.93×10^{-6} g m^{-3} s^{-1} in the weak run with weak fire intensity

753   through 2.01×10^{-6} g m^{-3} s^{-1} in the medium run with medium fire intensity by 74%. Those

754   averaged autoconversion rates reduce from 4.52×10^{-6} g m^{-3} s^{-1} in the low-aerosol run with

755   strong fire intensity to 3.94×10^{-6} g m^{-3} s^{-1} in the weak-low run with weak fire intensity

756   through 4.43×10^{-6} g m^{-3} s^{-1} in the medium-low run with medium fire intensity by 14%.

757   Associated with this, differences in the averaged autoconversion rates between the weak

758   run and the weak-low run for weak fire intensity are greater than those between the control

759   run and the low-aerosol run for strong fire intensity over period 2; differences in the

760   averaged autoconversion rates between the medium run and the medium-low run for

761   medium fire intensity are greater than those between the control run and the low-aerosol

762   run for strong fire intensity, and smaller than those between the weak run and the weak-

763   low run for weak fire intensity during period 2 (Figure 15a).

764   Due to smaller autoconversion rates, there is more cloud liquid available for freezing

765   in the control run than in the low-aerosol run for strong fire intensity, in the medium run

766   than in the medium-low run for medium fire intensity, and in the weak run than in the

767   weak-low run for weak fire intensity, respectively, particularly during period 2. Hence, the

768   rate of cloud-liquid freezing, which is averaged over cloudy areas and period 2, is greater

769   in the control run than in the low-aerosol run, in the medium run than in the medium-low

770   run, and in the weak run than in the weak-low run, respectively (Figure 15a). Remember

771   that the control run for strong fire intensity, the medium run for medium fire intensity and

772   the weak run for weak fire intensity constitute the polluted-scenario runs with higher

773   aerosol concentrations over the fire spot, and the low-aerosol run for strong fire intensity,

774   the medium-low run for medium fire intensity and the weak-low run for weak fire intensity

775   constitute the clean-scenario runs with lower aerosol concentrations over the fire spot.

776   Differences in autoconversion rates between the polluted-scenario run and the clean-

777   scenario run, which increase with weakening fire intensity, induce those differences in the

778   amount of cloud liquid available for freezing to get greater with weakening fire intensity

779   (Figure 15a). Thus, differences in the averaged rate of cloud-liquid freezing between the

780   polluted-scenario run and the clean-scenario run over period 2 gets greater with weakening

781   fire intensity (Figure 15a). Due to this, differences in freezing-related latent heat between

782   the runs increase with weakening fire intensity. When fire intensity is strong, the difference

783   in freezing-related latent heat, which is averaged over cloudy areas and period 2, between

784   the polluted-scenario run, which is the control run, and the clean-scenario run, which is the

785   low-aerosol run, is 1.60×10^{-4} J m^{-3} s^{-1}. However, with medium fire intensity, that difference

786   between the polluted-scenario run, which is the medium run, and the clean-scenario run,

787   which is the medium-low run, is 6.98×10^{-4} J m^{-3} s^{-1}, while with weak fire intensity, that

788   difference between the polluted-scenario run, which is the weak run, and the clean-scenario

789   run, which is the weak-low run, is 7.94×10^{-4} J m^{-3} s^{-1}. This corresponds to the variation of

790   the percentage differences, which are calculated by Equation (1), in the averaged freezing-

791   related latent heat between the polluted-scenario run and the clean-scenario run from 9%

792   with strong fire intensity to 83% with weak fire intensity through 51% with medium fire

793   intensity over the period 2.

794   As shown in Lee et al. (2017), enhanced freezing-related latent heat strengthens

795   updrafts in places where freezing occurs and this, in turn, enhances deposition and

796   deposition-related latent heat. Hence, although deposition, which is averaged over cloudy

797   areas and period 2, is slightly lower, due to those strengthened updrafts, the averaged

798   deposition and deposition-related latent heat are greater in the control run than in the low-

799   aerosol run for strong fire intensity, in the medium run than in the medium-low run for

800   medium fire intensity, and in the weak run than in the weak-low run for weak fire intensity,

801   respectively, during period 3 (Figures 15a and 15b). As seen in Figure 16, differences in

802   the averaged freezing rate (and thus the averaged freezing-related latent heating) over

803   cloudy areas between the control run and the low-aerosol run for strong fire intensity,

804   between the medium run and the medium-low run for medium fire intensity, and between

805   the weak run and the weak-low run for weak fire intensity, respectively, do not change

806   much up to ~20:30 GMT after they start to appear around 18:30 GMT. However, after

807   ~20:30 GMT, these differences start to increase as time goes by for each fire intensity. This

808   is because as convection intensifies, the transportation of cloud liquid to places above the

809   freezing level starts to be effective around 20:30 GMT. The greater freezing and thus

810   freezing-related latent heat in the control run than in the low-aerosol run, in the medium

811   run than in the medium-low run, and in the weak run than in the weak-low run, respectively,

812   which start to be significant around 20:30 GMT as compared to those before 20:30 GMT,

813   invigorates updrafts, which are represented by the averaged updraft mass fluxes over cloud

814   areas. This subsequently causes updrafts to be stronger in the control run than in the low-

815   aerosol run for strong fire intensity, in the medium run than in the medium-low run for

Atmospheric
Chemistry
and Physics
Discussions

Open Access

EGU

816 medium fire intensity, and in the weak run than in the weak-low run for weak fire intensity,

817 respectively, from ~21:00 GMT on (Figure 16). Then, the stronger updrafts induce

818 deposition, which is averaged over cloudy areas, to be greater in the control run than in the

819 low-aerosol run for strong fire intensity, in the medium run than in the medium-low run for

820 medium fire intensity, and in the weak run than in the weak-low run for weak fire intensity,

821 respectively. This is around 10-20 minutes after the stronger updrafts in the control run

822 than in the low-aerosol run, in the medium run than in the medium-low run, and in the

823 weak run than in the weak-low run, respectively, start to occur (Figure 16). Note that

824 deposition-related latent heat is about one order of magnitude greater than freezing-related

825 latent heat for a unit of mass of hydrometeors involved in phase-transition processes. This

826 contributes to much greater differences in deposition-related latent heat during period 3

827 than those in freezing-related latent heat between the control run and the low-aerosol run

828 for strong fire intensity, between the medium run and the medium-low run for medium fire

829 intensity, and between the weak run and the weak-low run for weak fire intensity,

830 respectively, during periods 2 or 3 (Figures 15a and 15b). To satisfy mass conservation,

831 the enhanced updrafts above the freezing level, due to enhanced freezing and deposition,

832 induce more updraft mass fluxes below the freezing level in the control run than in the low-

833 aerosol run for strong fire intensity, in the medium run than in the medium-low run for

834 medium fire intensity, and in the weak run than in the weak-low run for weak fire intensity,

835 respectively. This leads to more convergence around and below cloud base, which is air

836 flow from environment to cloud, in the control run than in the low-aerosol run for strong

837 fire intensity, in the medium run than in the medium-low run for medium fire intensity, and

838 in the weak run than in the weak-low run for weak fire intensity, respectively. The more

839 mass fluxes and the more convergence below the freezing level, in turn, enhance

840 condensation. Hence, condensation, which is averaged over cloud areas, starts to be greater

841 when time reaches ~22:30 GMT in the control run than in the low-aerosol run for strong

842 fire intensity, in the medium run than in the medium-low run for medium fire intensity, and

843 in the weak run than in the weak-low run for weak fire intensity, respectively (Figure 16).

844 This induces the averaged condensation and condensation-related latent heat to be greater

845 in the control run than in the low-aerosol run for strong fire intensity, in the medium run

846 than in the medium-low run for medium fire intensity, and in the weak run than in the

847   weak-low run for weak fire intensity, respectively, during period 4 (Figure 15c). Enhanced

848   condensation in turn enhances updrafts, establishing a feedback between freezing,

849   deposition, condensation, and updrafts and thus, enhancing freezing, deposition,

850   condensation, and updrafts further. This enhancement due to feedback eventually

851   determines the overall differences in the pyroCb properties and their impacts on the UTLS

852   water vapor and cloud ice between the control run and the low-aerosol run for strong fire

853   intensity, between the medium run and the medium-low run for medium fire intensity, and

854   between the weak run and the weak-low run for weak fire intensity, respectively.

855   Differences in freezing-related latent heat between the polluted-scenario run and the

856   clean-scenario run increase with weakening fire intensity, particularly during period 2.

857   Recall that the control run for strong fire intensity, the medium run for medium fire

858   intensity and the weak run for weak fire intensity are the polluted-scenario runs, while the

859   low-aerosol run for strong fire intensity, the medium-low run for medium fire intensity and

860   the weak-low run for weak fire intensity are the clean-scenario runs. Thus, percentage

861   differences in freezing-affected updrafts and subsequently in deposition-related latent heat,

862   which is averaged over cloudy areas and period 3, between the polluted-scenario run and

863   the clean-scenario run also increase with weakening fire intensity (Figures 15a, 15b and

864   16). Those differences, as calculated by Equation (1), in deposition-related latent heat are

865   16%, 181%, and 417 % for strong, medium, and weak fire intensity, respectively, as seen

866   in Figures 15b and 16. Since percentage increases in deposition-related latent heat in the

867   polluted-scenario run get greater with weakening fire intensity, the subsequent percentage

868   increases in updrafts in the polluted-scenario run as compared to updrafts in the clean-

869   scenario run get greater with weakening fire intensity, particularly during period 3 (Figure

870   16). During period 4, due to these greater increases in updrafts in the polluted-scenario run

871   with weaker fire intensity, the percentage increases in condensation in the polluted-

872   scenario run as compared to condensation in the clean-scenario run get greater with

873   weakening fire intensity (Figures 15c and 16). Then, the increases in condensation, in turn,

874   further enhance the increases in updrafts in the polluted-scenario run for each fire intensity.

875   This enhancement is greater with weaker fire intensity due to the greater increases in

876   condensation with weaker fire intensity. This leads to the greater overall effects of the

877   pyroCb on the UTLS water vapor and ice with weaker fire intensity.

Atmospheric
Chemistry
and Physics
Discussions

Open Access

EGU

30

878

4.2 Dependence of aerosol effects on the magnitude of aerosol perturbation

880

881   Table 3 shows that for each of the strong-, medium-, and weak-fire cases, there are

882   increases in the UTLS water-vapor mass and in the UTLS amount of cirrus clouds in the

883   run with the fire-induced aerosol perturbations of 30000 or 7500 cm^{-3}. These increases are

884   relative to the mass and the amount in the low-aerosol run for the strong-fire case, in the

885   medium-low run for the medium-fire case, and in the weak-low run for the weak-fire case,

886   respectively, with no fire-induced aerosol perturbation. Note that for each of the three types

887   of fire-induced aerosol perturbations of 30000, 15000 and 7500 cm^{-3}, aerosol-perturbation-

888   induced percentage increases in the UTLS water-vapor mass and the amount of UTLS

889   cirrus clouds get greater as fire intensity weakens (Tables 2 and 3). The qualitative nature

890   of results regarding the dependence of the percentage increases in the UTLS water-vapor

891   mass and the amount of UTLS cirrus clouds on fire intensity thus does not depend on the

892   magnitude of the fire-induced aerosol perturbation.

893   Until now, we considered the situation where the fire-induced aerosol perturbation

894   does not vary with fire intensity. Note that so far, we have taken interest in the sensitivity

895   to fire intensity of an aerosol perturbation on pyroCb development, UTLS water vapor,

896   and cirrus clouds. Hence, to examine and isolate the sensitivity, we have shown

897   comparisons among sensitivity simulations by varying only the fire intensity while

898   maintaining a constant aerosol perturbation. While working well for the isolation aspect,

899   this strategy does not reflect reality well. It may be that weaker fire intensity produces a

900   smaller aerosol concentration. This possibility is not that unrealistic, since stronger fire

901   likely involves more material burnt and more aerosols from it.

902   With this situation in mind, we make comparisons among three pairs of simulations:

903   the low-aerosol run and the control-30000 run for strong fire vs. the medium-low run and

904   the medium run for medium fire vs. the weak-low run and the weak-7500 run for weak fire.

905   Hence, among these three pairs, the magnitude of fire-induced aerosol perturbation reduces

906   with weakening fire, emulating the possibility that weaker fire intensity involves a less

907   amount of aerosols. For strong fire, the perturbation-related aerosol concentration is 30000

908   cm^{-3}, for medium fire, it is 15000 cm^{-3}, and for weak fire, it is 7500 cm^{-3}. As shown in

909   Tables 2 and 3, comparisons among these three pairs show that relative importance of

910   aerosol effects on the pyroCb development and its impacts on UTLS water vapor and cirrus

911   clouds increases for weaker fires, and it does not matter if the aerosol perturbation reduces

912   or stays constant with weakening fire intensity. In these comparisons, it is also possible

913   that when fire-induced aerosol perturbation is very low for medium or weak fire intensity,

914   the latent heat perturbation by aerosol perturbation can be very low. This very low latent

915   heat is not large enough to increase the relative importance of those aerosol effects with

916   weakening fire intensity. Based on this, the medium run and the weak run are repeated

917   again. The medium run is repeated with lower fire-induced aerosol perturbations than the

918   perturbation of 15000 cm^{-3}, while the weak run is repeated with lower fire-induced aerosol

919   perturbations than the perturbation of 7500 cm^{-3}. Recall that when the repeated medium

920   run has the aerosol perturbation of 2000 cm^{-3}, the repeated medium run is referred to as the

921   medium-2000 run; when the repeated weak run has the aerosol perturbation of 1000 cm^{-3},

922   the repeated weak run is referred to as the weak-1000 run. The percentage increases in the

923   UTLS water vapor and the cirrus-cloud amount from the medium-low run to the medium-

924   2000 run or from the weak-low run to the weak-1000 run are smaller than those increases,

925   for the case of strong fire, from the low-aerosol run to the control-30000 run. This indicates

926   that when fire-induced aerosol perturbation reduces too much with weakening fire intensity,

927   the relative importance of aerosol effects on pyroCb development and its impacts on the

928   UTLS water vapor and cirrus clouds no longer increases with the weakening fire intensity.

929

930   ## 5. Summary and conclusion

931

932   This study investigates an observed case of a pyroCb using a modeling framework. In

933   particular, this study focuses on effects of fire-produced aerosols on pyroCb development

934   and its impacts on the UTLS water vapor and cirrus clouds. Results show that pyroCb

935   updrafts transport water vapor to the tropopause and above efficiently. This leads to a much

936   greater amount of water vapor around and above the tropopause (i.e., the UTLS) over the

937   pyroCb as compared to that in the background outside the pyroCb. The pyroCb also

938   generates a deck of cirrus cloud around the tropopause. It is found that the role played by

939   fire-produced aerosols or the fire-induced aerosol perturbation in the water-vapor

940   transportation to UTLS and the production of cirrus cloud in the pyroCb gets more

941   significant as fire intensity weakens.

942   As fire intensity weakens, due to the reduction in LWC, R_v decreases despite the

943   reduction in CDNC that tends to increase R_v. During the initial stage, there is a similar

944   LWC between the polluted-scenario run (i.e., the control run for strong fire intensity, the

945   medium run for medium fire intensity and the weak run for weak fire intensity with the

946   fire-induced aerosol perturbation) and the clean-scenario run (i.e., the low-aerosol run for

947   strong fire intensity, the medium-low run for medium fire intensity and the weak-low run

948   for weak fire intensity with no fire-induced aerosol perturbation) for each fire intensity.

949   The reduction in LWC with weakening fire intensity among the polluted-scenario runs (i.e.,

950   the control run, the medium run and the weak run) is also similar to that among the clean-

951   scenario runs (i.e., the low-aerosol run, the medium-low run and the weak-low run). During

952   the initial stage, there are much greater CDNC in the polluted-scenario run than in the

953   clean-scenario run for each fire intensity, and the smaller CDNC reduction among the

954   polluted-scenario runs than among the clean-scenario runs with weakening fire intensity.

955   This situation during the initial stage induces R_v to reduce much more among the polluted-

956   scenario runs than among the clean-scenario runs with weakening fire intensity. This

957   reduces autoconversion more among the polluted-scenario runs than among the clean-

958   scenario runs with weakening fire intensity. This makes differences in autoconversion

959   between the polluted-scenario run and the clean-scenario run enhance as fire intensity

960   weakens. The enhancing difference in autoconversion between the polluted-scenario run

961   and the clean-scenario run causes greater differences in freezing-related latent heat as fire

962   intensity weakens. Through feedback between freezing, deposition, updrafts, and

963   condensation, differences in freezing-related latent heat induce differences in updrafts

964   between the polluted-scenario run and the clean-scenario run. Those greater differences in

965   freezing-related latent heat also lead to greater differences in updrafts, producing the

966   greater differences in the UTLS water vapor and cirrus clouds between the runs with

967   weaker fire intensity. This means that the role of fire-produced aerosols in water-vapor

968   transport to the UTLS and the production of cirrus cloud in the pyroCb becomes more

969   significant as fire intensity weakens. This role which is more significant with weaker fire

970   intensity is robust to the magnitude of the given fire-induced aerosol perturbation which

971   was assumed not to vary with varying fire intensity. This more significant role with weaker

972   fire intensity is also robust to the variation of the fire-induced aerosol perturbation with the

973   varying fire intensity unless the variation is very high.

974   It is true that the level of the understanding of a mechanism that controls the role

975   played by fire-produced aerosols in the development of pyroCbs and their impacts on water

976   vapor and cirrus clouds in the UTLS has been low. This study shows that fire-produced

977   aerosols can invigorate convection and updrafts and thus cause enhanced transportation of

978   water vapor to the UTLS and enhanced formation of cirrus clouds. This study finds that

979   the mechanism that controls the invigoration of convection by aerosols in the pyroCb is

980   consistent with the traditional invigoration mechanism which was proposed and detailed in

981   Rosenfeld et al. (2008). However, this study shows that for pyroCbs produced by strong

982   fires, the aerosol-induced invigoration and its effects on water vapor and cirrus clouds in

983   the UTLS are insignificant. Note that traditional understanding generally focuses on effects

984   of fire-produced heat and water vapor and their associated fluxes around the surface on the

985   pyroCb and does not consider effects of fire-produced aerosols on the pyroCb, and this

986   understanding adequately explains the mechanics for pyroCbs in association with strong

987   fires. However, this study suggests that the role of fire-produced aerosols in pyroCb

988   development and its effects on the UTLS water vapor and cirrus clouds should be

989   considered for cases where pyroCbs form over weak-intensity fires, should one be observed

990   in nature.

991   It is of interest to note that when fire-induced aerosol perturbations are strongly

992   reduced for cases of weaker-intensity fires compared with strong-intensity fires, the

993   significance of the role played by fire-produced aerosol perturbation does not increase any

994   longer and starts to reduce with weakening fire. This suggests that there is a critical level

995   of aerosol perturbation below which the increase in the significance with weakening fire

996   intensity ceases.

997

998

999

1000

1001

Atmospheric
Chemistry
and Physics
Discussions

1002 **Author contributions**

1003 SSL came up with the research goals and aims, preformed the simulations, and wrote the

1004 manuscript. GK and ZL selected the case, analyzed observations, and provided data to set

1005 up the simulations while reviewing and providing comments on the manuscript.

1006

1007 **Acknowledgements**

1010

1011

1012

1013

1014

1015

1016

1017

1018

1019

1020

1021

1022

1023

1024

1025

1026

1027

1028

1029

1030

1031

1032

References

Fouquart, Y., and Bonnel, B.: Computation of solar heating of the Earth's atmosphere: a new parameterization, Beitr. Phys. Atmos., 53, 35-62, 1980.

Houze, R. A.: Cloud dynamics, Academic Press, 573 pp, 1993.

Kablick, G., Fromm, M., Miller, S., Partain, P., Peterson. D., Lee, S. S., Zhang, Y., Lambert, A., and Li, Z.: The Great Slave Lake pyroCb of 5 August 2014: observations, simulations, comparisons with regular convection, and impact on UTLS water vapor, J. Geophy. Res., https://doi.org/10.1029/2018JD028965, 2018.

Khain, A., Ovtchinnikov, M., Pinsky, M.: Notes on the state-of-the-art numerical modeling of cloud microphysics, Atmos. Res., 55, 159-224, 2000.

Khain, A.: Notes on state-of-the-art investigations of aerosol effects on precipitation: a critical review, Environ. Res. Lett., 4, doi:10.1088/1748-9326/4/1/015004, 2009.

Khain, A., BenMoshe, N., and Pokrovsky, A.: Factors determining the impact of aerosols on surface precipitation from clouds: Attempt of classification, J. Atmos. Sci., 65, 1721-1748, 2008.

Khairoutdinov, M., and Kogan, Y.: A new cloud physics parameterization in a large-eddy simulation model of marine stratocumulus, Mon. Wea. Rev., 128, 229-243, 2000.

Knobelspiesse, K., Cairus, B., Ottaviani, M., et al.: Combined retrievals of boreal forest fire aerosol properties with a polarimeter and lidar, Atmos. Chem. Phys., 11, 7045-7067, 2011.

Koop, T., Luo, B. P, Tsias, A. and Peter, T,: Water activity as the determinant for homogeneous ice nucleation in aqueous solutions, Nature, 406, 611-614. 2000.

Koren, I., Altaratz, O., Remer, L. A., et al.: Aerosol-induced intensification of rain from the tropics to the mid-latitudes, Nat. Geosci., 5, 118-122, 2012.

Lee, H., and Baik, J.-J.: A physically based autoconversion parameterization, J. Atmos. Sci., 74, 1599-1615, 2017.

Lee, S. S., Donner, L. J., Phillips, V. T. J., and Ming, Y.: The dependence of aerosol effects on clouds and precipitation on cloud-system organization, shear and stability, J. Geophys. Res., 113, D16202, 2008.

Lee, S. S., Feingold, G., Koren, I., Yu, H., Yamaguchi, T., and McComiskey, A.: Effect of

1064   gradients in biomass burning aerosol on circulations and clouds, J. Geophys. Res.,

1065   119, 9948-9964, 2014.

1066   Lee, S. S., Li, Z., and Mok, J., et al.: Interactions between aerosol absorption,

1067   thermodynamics, dynamics, and microphysics and their impacts on clouds and

1068   precipitation in a multiple-cloud system, Clim. Dyn., 49, 3905-3921, 2017.

1069   Lee, S. S., and Penner, J. E.: Comparison of a global-climate model to a cloud-system

1070   resolving model for the long-term response of thin stratocumulus clouds to

1071   preindustrial and present-day aerosol conditions, Atmos. Chem. Phys., 10, 6371-6389,

1072   2010.

1073   Lee, S. S., Penner, J. E., and Saleeby, S. M.: Aerosol effects on liquid-water path of thin

1074   stratocumulus clouds., J. Geophys. Res., 114, D07204, 2009.

1075   Liu, Y., and Daum, P. H.: Parameterization of the autoconversion process. Part I: Analytical

1076   formulation of the Kessler-type parameterizations, J. Atmos. Sci., 61, 1539-1548,

1077   2004.

1078   Lohmann, U. and Diehl, K.: Sensitivity studies of the importance of dust ice nuclei for the

1079   indirect aerosol effect on stratiform mixed-phase clouds, J. Atmos. Sci., 63, 968-982,

1080   2006.

1081   Luderer, G., Trentmann, J., Winterrath, T., Textor, C., Herzog, M., Graf, H., and Andreae,

1082   M.: Modeling of biomass smoke injection into the lower stratosphere by a large forest

1083   fire (part ii): Sensitivity studies. Atmos. Chem. Phy., 6, 5261–5277, 2006.

1084   Mlawer, E. J., Taubman, S. J., Brown, P. D., Iacono, M. J., and Clough, S. A.: RRTM, a

1085   validated correlated-k model for the longwave, J. Geophys. Res., 102, 16663-1668,

1086   1997.

1087   Möhler, O., et al.: Efficiency of the deposition mode ice nucleation on mineral dust particles,

1088   Atmos. Chem. Phys., 6, 3007-3021, 2006.

1089   Pruppacher, H. R., and Klett, J. D.: Microphysics of clouds and precipitation, 714pp, Reidel

1090   D., 1978.

1091   Reid, J. S., Hobbs, P. V., Rangno, A. L., and Hegg, D. A.: Relationships between cloud

1092   droplet effective radius, liquid water content, and droplet concentration for warm

1093   clouds in Brazil embedded in biomass smoke, J. Geophys. Res., 104, 6145-6153, 1999.

1094   Reid, J. S., Koppmann, R., Eck T. F., and Eleuterio, D.: A review of biomass burning

1095   emissions part II: intensive physical properties of biomass burning particles, Atmos.
1096   Chem. Phys., 5,799-825, 2005.

1097   Rogers, R. R., and Yau, M. K.: A short course in cloud physics, Pergamon Press, 293pp,
1098   1991.

1099   Rosenfeld, D., Lohmann, U., Raga, G. B., et al.: Flood or drought, How do aerosols affect
1100   precipitation? Science, 321, 1309-1313, 2008.

1101   Solomon, S., Rosenlof, K. H., Portmann, R. W., Daniel, J. S., Davis, S. M., Sanford, T. J.,
1102   and Plattner, G. K.: Contributions of stratospheric water vapor to decadal changes in
1103   the rate of global warming, Science, 327, 1219–1223, 2010.

1104   Storer, R. L., van den Heever, S. C., and Stephens, G. L.: Modeling aerosol impacts on
1105   convection under differing storm environments, J. Atmos. Sci., 67, 3904-3915, 2010.

1106   Tao, W.-K., Chen, J.-P., Li, Z., Wang, C., and Zhang, C.: Impact of aerosols on convective
1107   clouds and precipitation, Rev. Geophys., 50, RG2001, 2012.

1108   Trentmann, J., Luderer, G., Winterrath, T., Fromm, M., Servranckx, R., Textor, C., et al.:
1109   Modeling of biomass smoke injection into the lower stratosphere by a large forest fire
1110   (part i): reference simulation. Atmos. Chem. Phy., 6, 5247–5260.

1111   Wang, H., Skamarock, W. C., and Feingold, G.: Evaluation of scalar advection schemes in
1112   the Advanced Research WRF model using large-eddy simulations of aerosol-cloud
1113   interactions, Mon. Wea. Rev., 137, 2547-2558, 2009.

1114
1115
1116
1117
1118
1119
1120
1121
1122
1123
1124
1125
1126
1127
1128
1129
1130
1131

38

FIGURE CAPTIONS

Figure 1. VIIRS visible image of fire, smoke and cirrus cloud which are associated with the selected pyroCb. The bright white represents cirrus cloud or anvil cloud at the top of the pyroCb, while the red circle marks the fire spot. The dark white represents smoke produced by fire. Adapted from Kablick et al. (2018).

Figure 2. The simulated fire spot and the field of cloud-ice mass density at the top of the simulated pyroCb when the pyroCb is about to advance to its mature stage. The red circle marks the simulated fire spot, while the field represents the simulated cirrus cloud.

Figure 3. Initial aerosol size distribution in the PBL over the fire spot. N represents aerosol number concentration per unit volume of air and D aerosol diameter.

Figure 4. The vertical distribution of the radar reflectivity which is averaged over the Cloudsat path.

Figure 5. Vertical distributions of the averaged updraft mass fluxes over cloudy areas, where the sum of liquid-water content (LWC) and ice-water content (IWC) is non-zero, and over the simulation period between 17:00 GMT on August 5th and 12:00 GMT on August 6th in the control run and the low-aerosol run.

Figure 6. Vertical distributions of the averaged water-vapor mass density in the control run and the low-aerosol run over altitudes above 13 km and over the simulation period between 17:00 GMT on August 5th and 12:00 GMT on August 6th. Colored lines represent the averaged values over cloudy grid columns where there is the non-zero sum of liquid-water path (LWP) and ice-water path (IWP) in the control run and the low-aerosol run, while the black line represents those values over non-cloudy columns where there is the zero sum of LWP and IWP in the control run.

Figure 7. Vertical distributions of the averaged cloud-ice mass density over cloudy areas, where the sum of liquid-water content (LWC) and ice-water content (IWC) is non-zero,

1164 and over the simulation period between 17:00 GMT on August 5th and 12:00 GMT on

1165 August 6th in the control run and the low-aerosol run.

1166

1167 Figure 8. Vertical distributions of the averaged deposition rate over cloudy areas and over

1168 the simulation period between 17:00 GMT on August 5th and 12:00 GMT on August 6th in

1169 the control run and the low-aerosol run.

1170

1171 Figure 9. Same as Figure 5 but for all three types of fire intensity.

1172

1173 Figure 10. Same as Figure 6 but for all three types of fire intensity.

1174

1175 Figure 11. Same as Figure 7 but for all three types of fire intensity.

1176

1177 Figure 12. The averaged CDNC, R_v, and LWC over cloudy areas at all altitudes and over

1178 period between 17:00 and 19:00 GMT on August 5th.

1179

1180 Figure 13. Graphic depiction of y values as a function of " $x^{\frac{1}{3}}$ ". x_{L1} and x_{L2} represent large

1181 x values, while x_{S1} and x_{S2} represent small x values. y values corresponding to x_{L1}, x_{L2}, x_{S1}

1182 and x_{S2} are y_{L1}, y_{L2}, y_{S1} and y_{S2}, respectively. The variation of x value from x_{L1} to x_{L2}, is

1183 greater than that from x_{S1} to x_{S2}.

1184

1185 Figure 14. Diagrammatic depiction of the varying minimum size of aerosol activation with

1186 varying fire intensity in the unimodal aerosol size distribution which is assumed in this

1187 study. The details of the varying minimum size are described in Section 4.1.2. D_{cs} and D_{cw}

1188 represent the minimum size in the low-aerosol run for strong fire intensity and in the weak-

1189 low run for weak fire intensity, respectively, while D_{ps} and D_{pw} represent the minimum size

1190 in the control run for strong fire intensity and in the weak run for weak fire intensity,

1191 respectively. Here, the variation of the minimum size from D_{cs} to D_{cw} is identical to that

1192 from D_{ps} to D_{pw}.

1193

1194   Figure 15. The averaged rates of condensation, deposition and cloud-liquid freezing over

1195   cloudy areas at all altitudes and over (a) periods 2, (b) period 3 and (c) period 4. In panel

1196   (a), the averaged autoconversion rates over cloudy areas at all altitudes and over periods 2

1197   is additionally shown.

1198

1199   Figure 16. Time series of differences in the averaged values of variables, which are related

1200   to aerosol-induced invigoration of convection, over cloudy areas at all altitudes (a) between

1201   the control run and the low-aerosol run for strong fire intensity, (b) between the medium

1202   run and the medium-low run for medium fire intensity and (c) between the weak run and

1203   the weak-low run for weak fire intensity.

1204

1205

1206

1207

1208

1209

1210

1211

1212

1213

1214

1215

1216

1217

1218

1219

1220

1221

1222

1223

1224

Atmospheric
Chemistry
and Physics
Discussions

Simulations	Surface sensible heat fluxes in the fire spot (W m^{-2})	Surface latent heat fluxes in the fire spot (W m^{-2})	Aerosol concentration in the PBL over the fire spot (cm^{-3})
Control run	15000	1800	15000
Low-aerosol run	15000	1800	150
Control-30000	15000	1800	30000
Control-7500	15000	1800	7500
Medium run	7500	900	15000
Medium-low run	7500	900	150
Medium-30000	7500	900	30000
Medium-7500	7500	900	7500
Medium-2000	7500	900	2000
Weak run	3750	450	15000
Weak-low run	3750	450	150
Weak-30000	3750	450	30000
Weak-7500	3750	450	7500
Weak-1000	3750	450	1000

1225

1226 Table 1. Summary of simulations

1227

1228

1229

1230

1231

1232

1233

1234

1235

1236

1237

1238

1239

1240

1241

1242

1243

1244

1245

1246

42

	Backg-round	Control	Low-aerosol	Differe-nce (%)	Medium	Meidum-low	Differe-nce (%)	Weak	Weak-low	Differe-nce (%)
Updraft mass fluxes (kg m^{-2} s^{-1})		1.23	1.19	3	0.89	0.70	27	0.42	0.21	100
Water-vapor mass density between 13 and 16 km (10^{-3} g m^{-3})	0.46	2.31	2.26	2	1.61	1.32	22	0.93	0.58	60
Cirrus-cloud mass density between 9 and 13 km (g m^{-3})		0.024	0.023	4	0.017	0.012	42	0.008	0.004	100

1247

1248   Table 2. The averaged updraft mass fluxes over cloudy areas at all altitudes, the averaged

1249   water-vapor mass density over altitudes between 13 and 16 km and over cloudy columns

1250   except for the averaged background water-vapor mass density which is also over altitudes

1251   between 13 and 16 km but over non-cloudy columns, and the averaged cirrus-cloud mass

1252   density over cloudy areas between 9 and 13 km. These averaged values are obtained over

1253   the simulation period between 17:00 GMT on August 5th and 12:00 GMT on August 6th.

1254   "Difference" is the percentage difference between the polluted-scenario run and the clean-

1255   scenario run for each fire intensity. Note that the control run for strong fire intensity, the

1256   medium run for medium fire intensity and the weak run for weak fire intensity constitute

1257   the polluted-scenario runs with higher aerosol concentrations over the fire spot, and the

1258   low-aerosol run for strong fire intensity, the medium-low run for medium fire intensity and

1259   the weak-low run for weak fire intensity constitute the clean-scenario runs with lower

1260   aerosol   concentrations   over   the   fire   spot.   The   percentage   difference   is

1261 $\frac{The\ polluted-scenario\ run\ minus\ the\ clean-scenario\ run}{The\ clean-scenario\ run} \times 100\ (\%)$.

1262

1263

1264

1265

1266

	Control-30000	Control-7500	Medium-30000	Medium-7500	Medium-2000	Weak-30000	Weak-7500	Weak-1000
Water vapor mass density between 13 and 16 km (10^{-3} g m^{-3})	2.38 (5%)	2.28 (0.9%)	1.87 (42%)	1.50 (14%)	1.36 (3%)	1.31 (125%)	0.75 (29%)	0.60 (3%)
Cirrus cloud mass density between 9 and 13 km (g m^{-3})	0.025 (9%)	0.023 (0.2%)	0.023 (92%)	0.014 (17%)	0.012 (3%)	0.013 (225%)	0.006 (50%)	0.004 (8%)

1267

1268   Table 3. The averaged water-vapor mass density over cloudy columns between 13 and 16

1269   km and, the averaged cirrus-cloud mass density over cloudy areas between 9 and 13 km.

1270   These averaged values are obtained over the simulation period between 17:00 GMT on

1271   August 5th and 12:00 GMT on August 6th. The number in parenthesis is the percentage

1272   difference   which   is $\frac{The\ control-30000\ (or\ the\ control-7500)\ run\ minus\ the\ low-aerosol\ run}{The\ low-aerosol\ run} \times$

1273   100 (%) for strong fire intensity,

1274 $\frac{The\ medium-30000\ (or\ the\ medium-7500\ or\ the\ medium-2000)\ run\ minus\ the\ medium-low\ run}{The\ medium-low\ run} \times$

1275   100 (%) for medium fire intensity, and

1276 $\frac{The\ weak-30000\ (or\ the\ weak-7500\ or\ the\ weak-1000)\ run\ minus\ the\ weak-low\ run}{The\ weak-low\ run} \times 100$ (%) for

1277   weak fire intensity.

1278

1279

44

1280

1281

Figure 1

Atmospheric
Chemistry
and Physics
Discussions

Open Access

EGU

45

Figure 2

1282
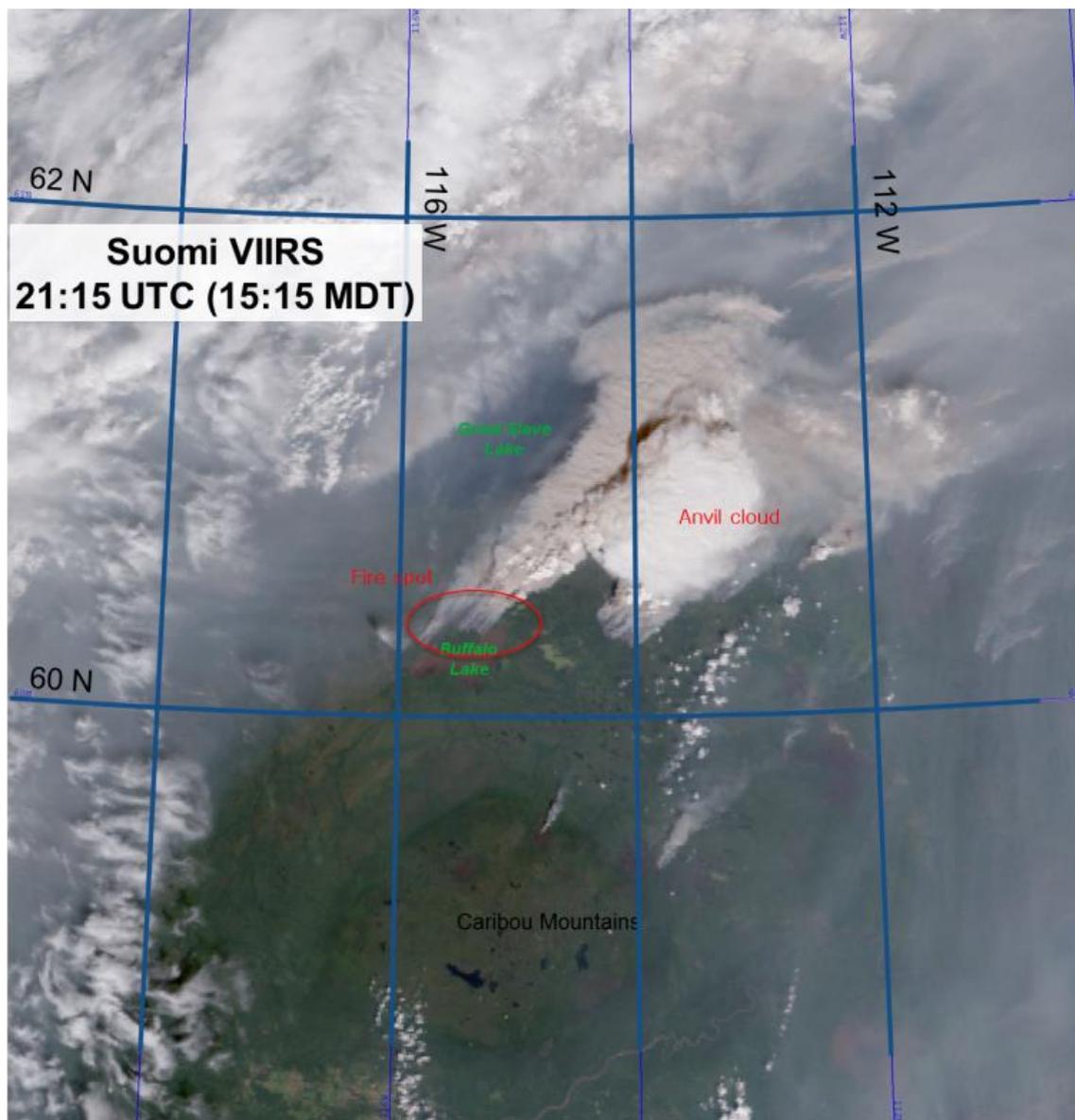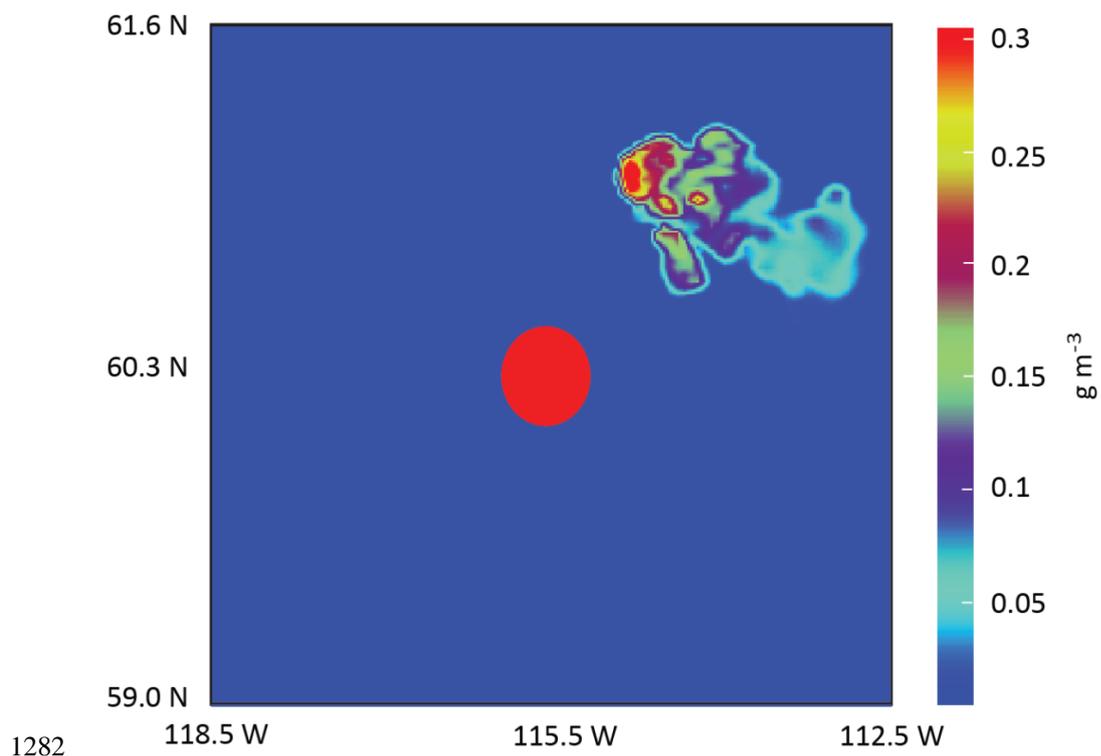
1283

1284

1285

1286

1287

1288

1289

1290

1291
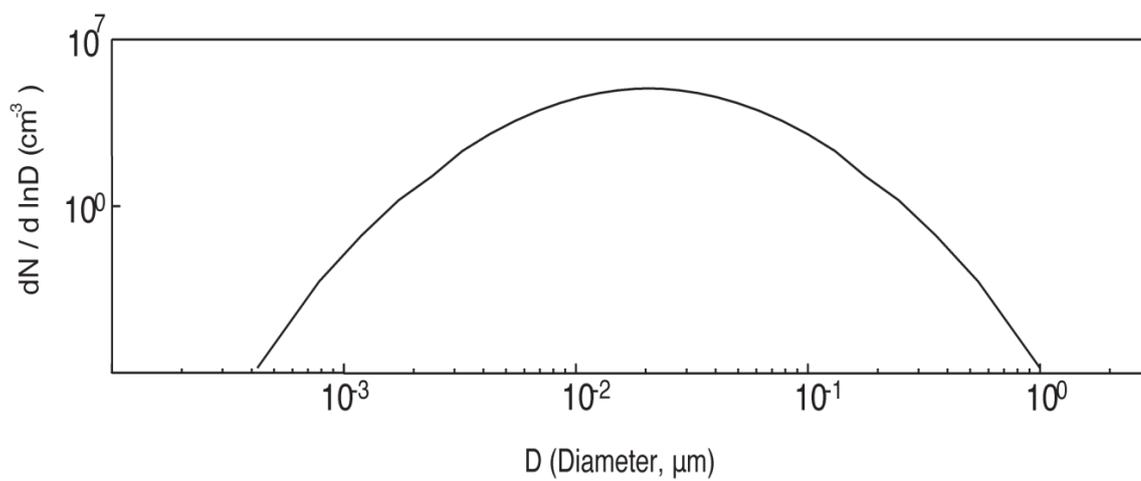
1292

Figure 3

1293

1294

1295

1296

1297

1298

1299

1300

1301

1302

47

1303

1304
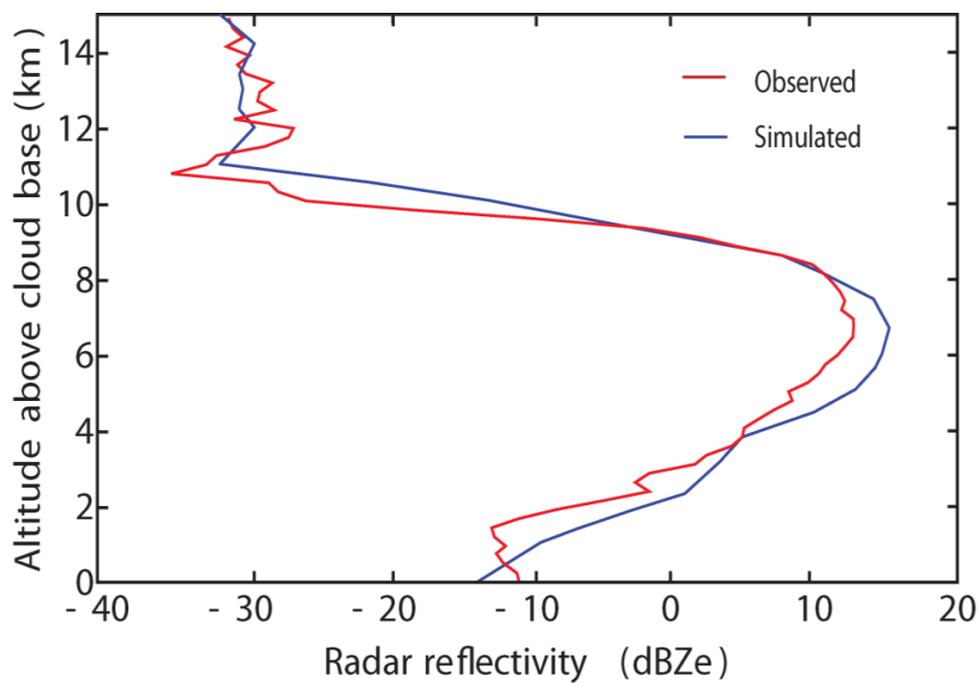
1305

Figure 4

1307

1308

1309

1310

1311

1312

1313

Atmospheric
Chemistry
and Physics
Discussions

Open Access

EGU

48

1314
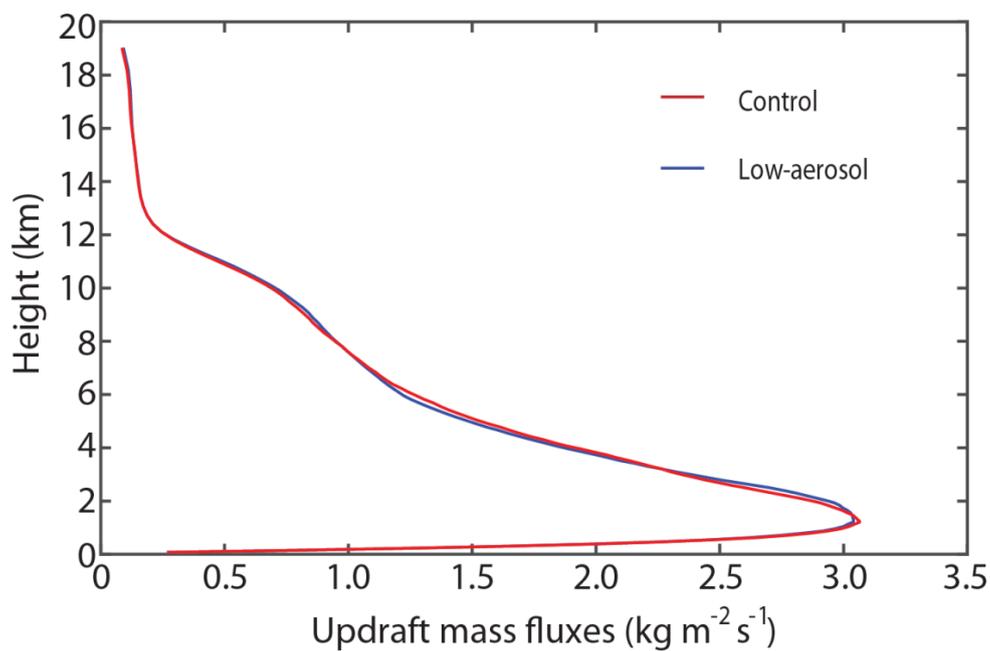
Figure 5

1315

Figure 5

1317

1318

1319

1320

1321

1322

1323

49
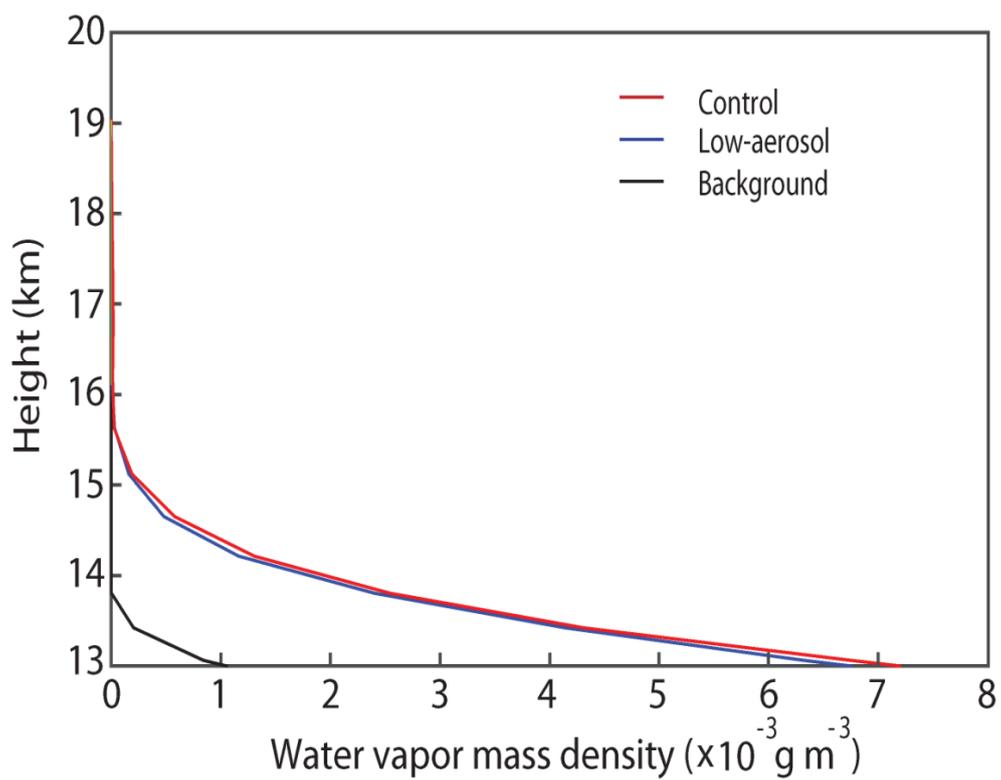
Figure 6

1324

1325

1326

1327

1328

1329

1330

1331

50
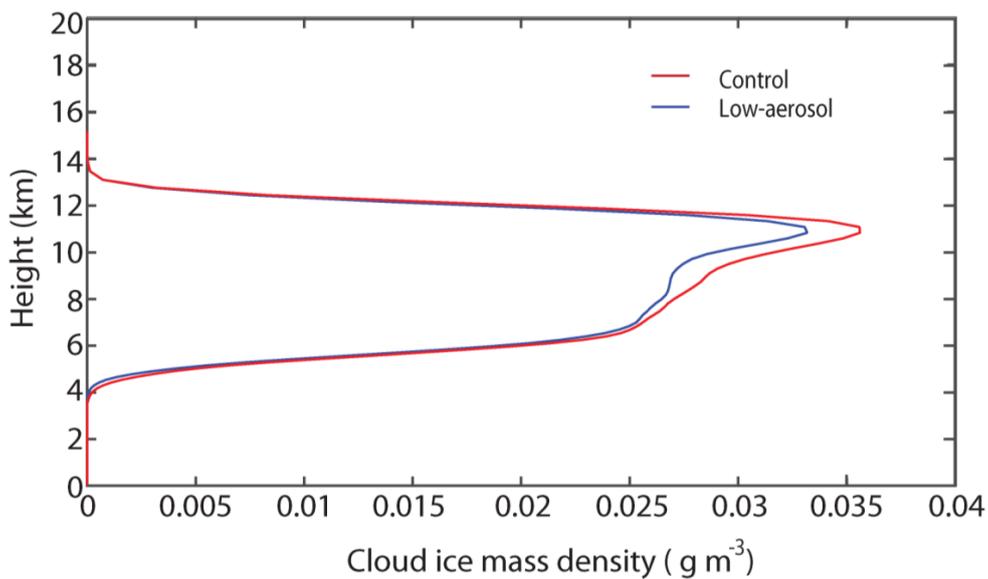
Figure 7

1332

1333

1334

1335

1336

1337

1338

1339

1340

1341

1342

51

1343

Figure 8

1344

1345

Atmospheric
Chemistry
and Physics
Discussions
Open Access
EGU

52
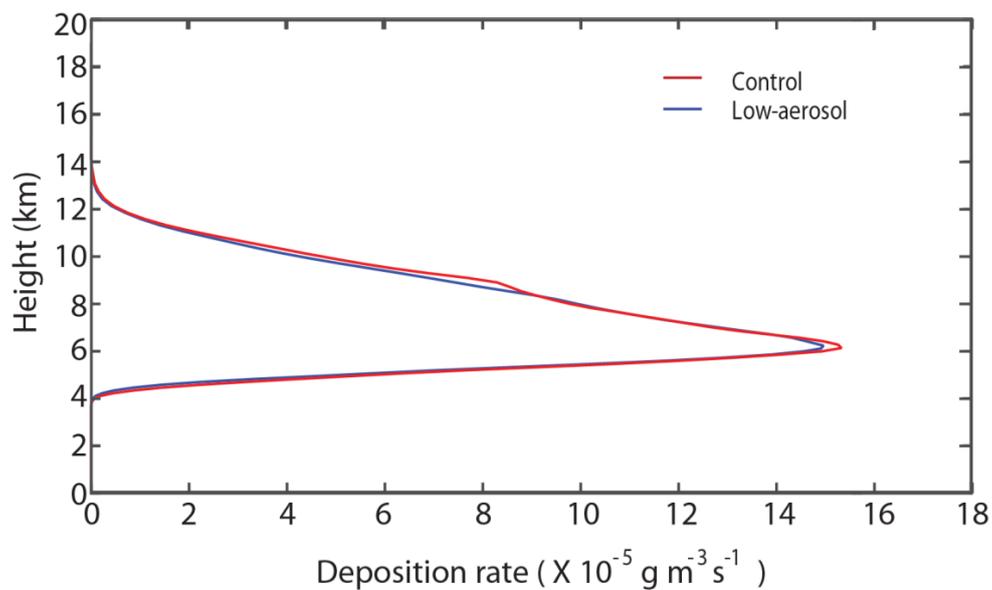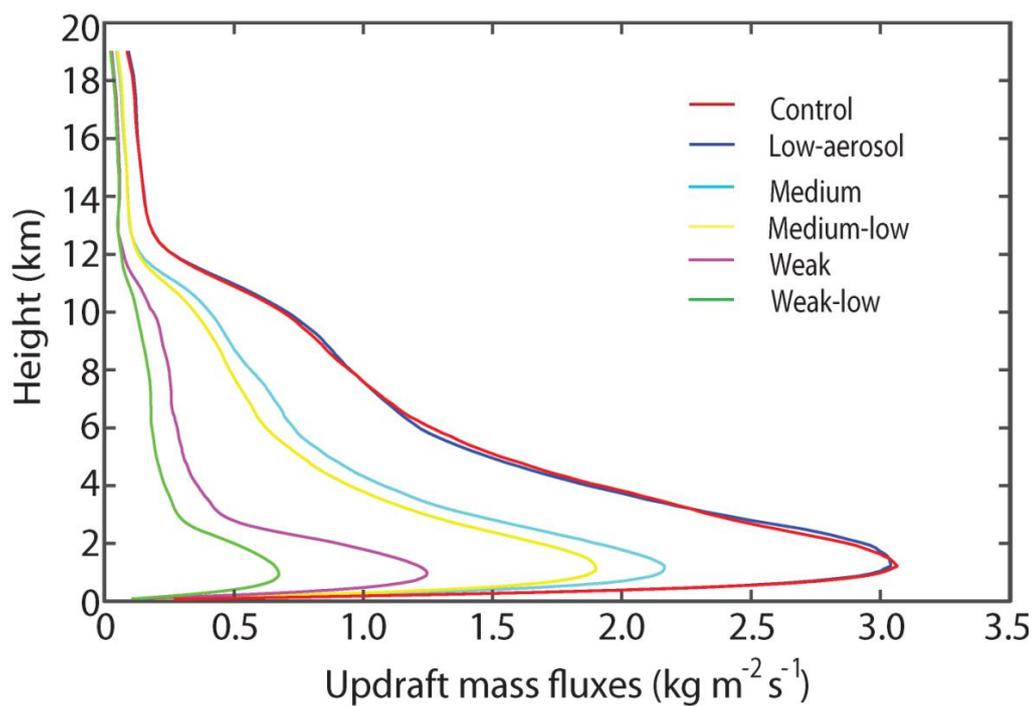
Figure 9

1346

1347

1348

1349

1350

1351

1352

1353

1354

1355

53
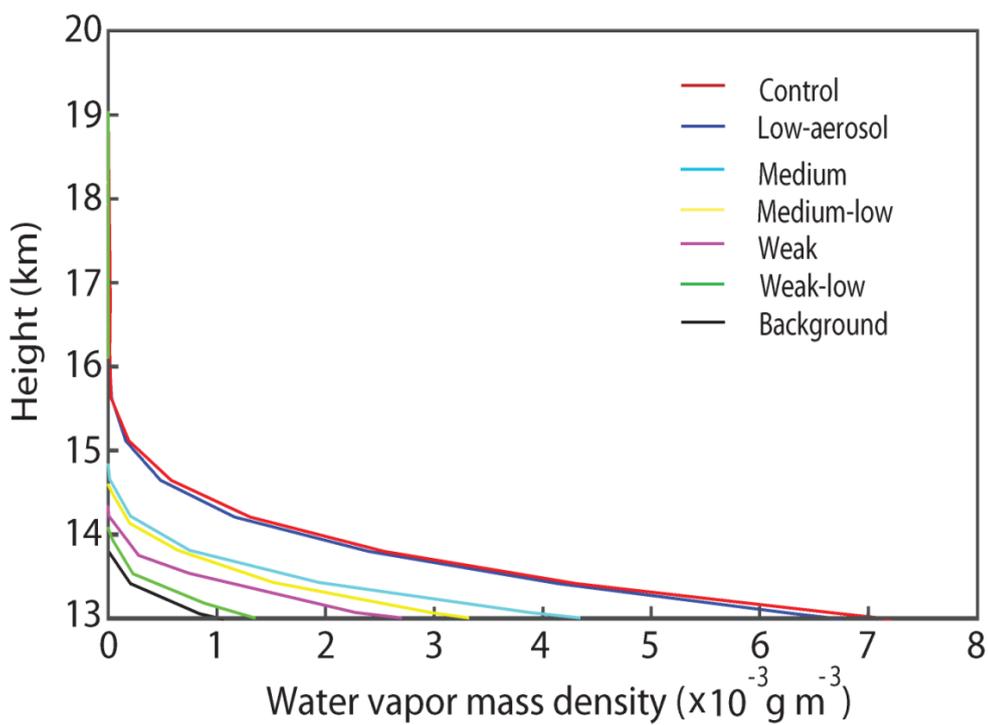
Figure 10

1356

1357

1358

1359

1360

1361

1362

1363

1364

1365

54
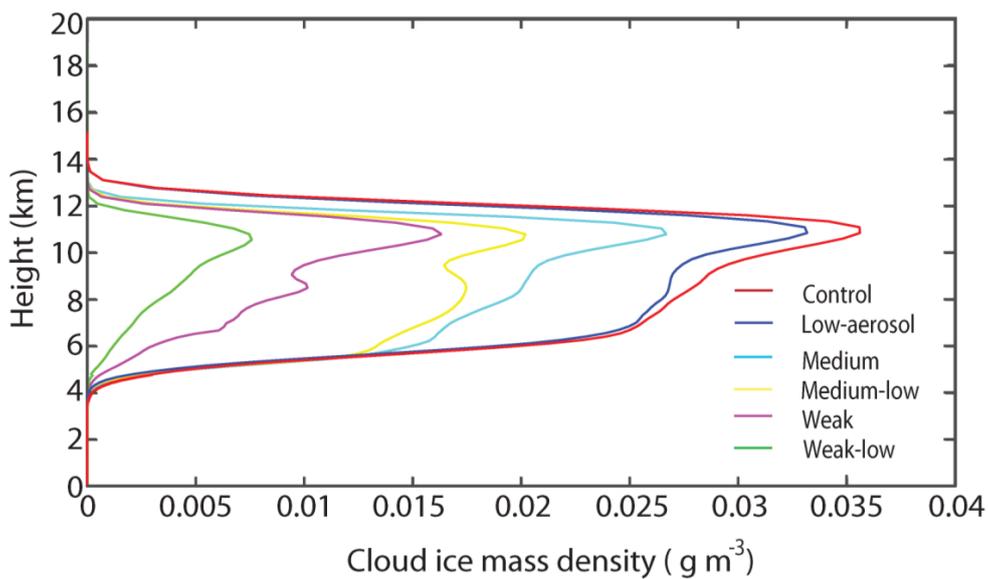
Figure 11

1366

1367

1368

1369

1370

1371

1372

1373

1374

1375

1376

55
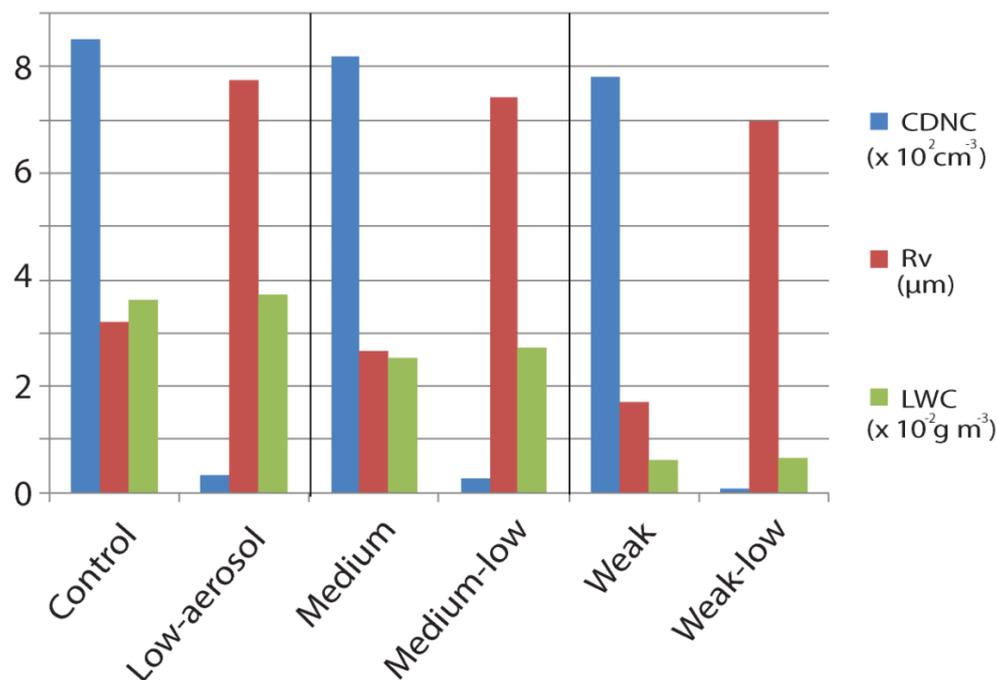
1377

Figure 12

1378

1379

1380

1381

1382

1383

1384

1385
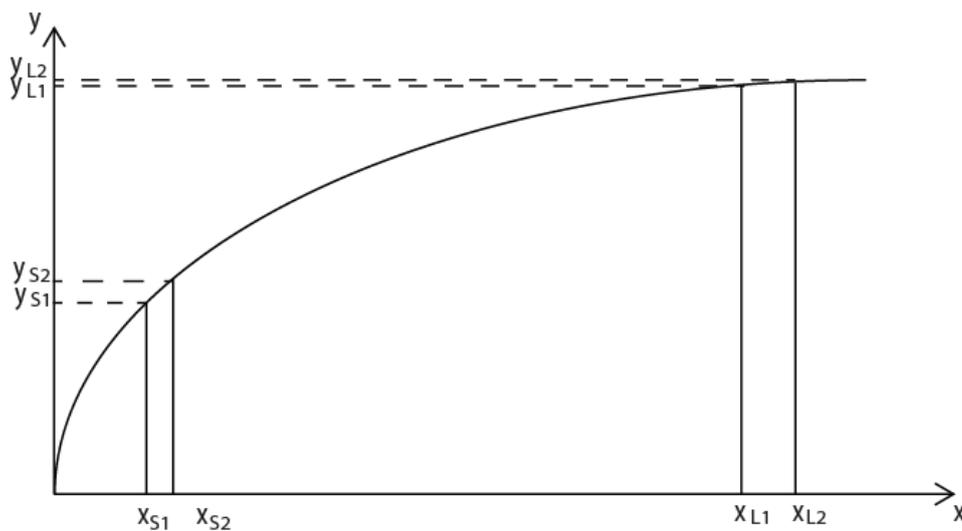
1386

Figure 13

1387

1388

1389

1390

1391

1392

1393

Atmospheric
Chemistry
and Physics
Discussions
Open Access
EGU
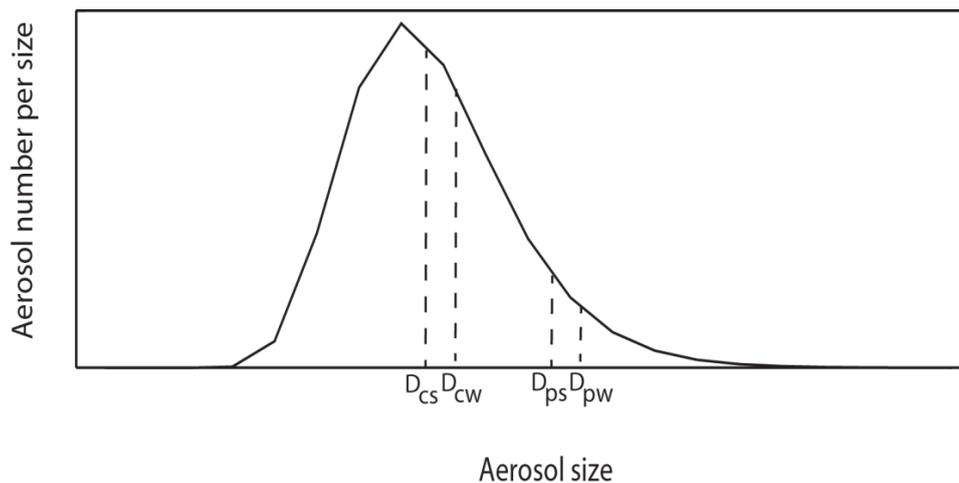
Figure 14

1394

1395

1396

1397

1398

1399

1400

1401

1402

1403

1404

1405
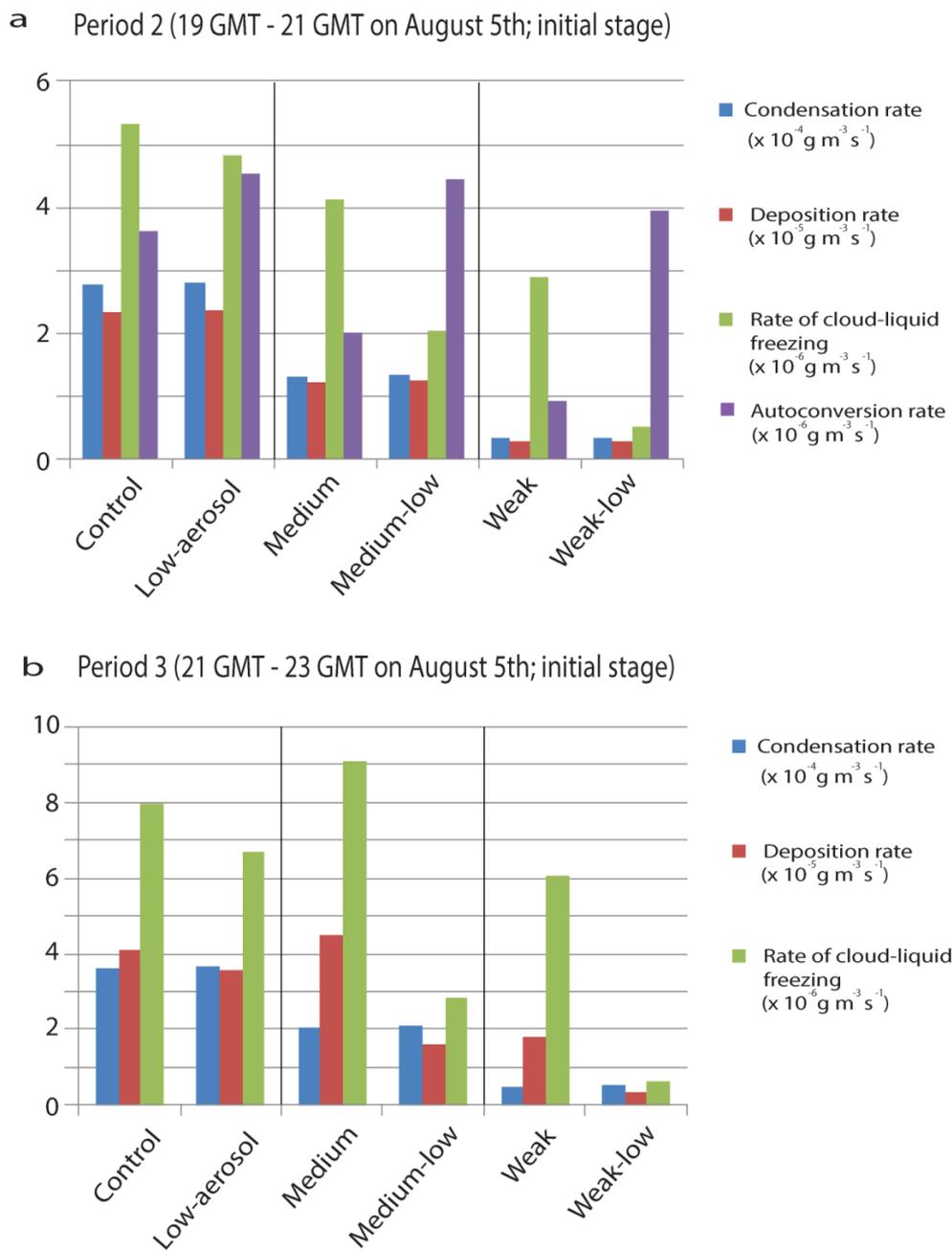
58

Figure 15

Figure 15

1409

1410

1411

1412

1413

1414

Figure 16

61
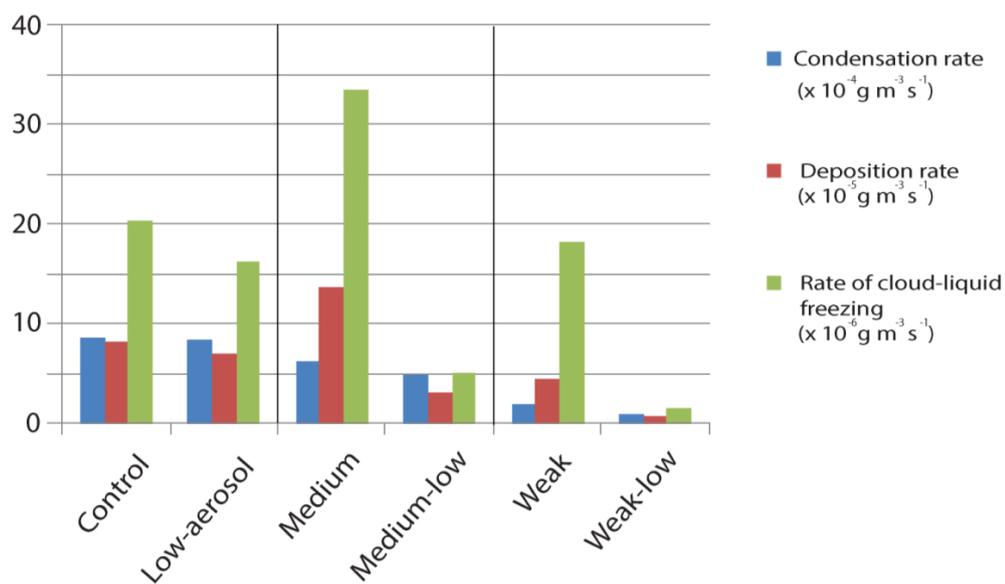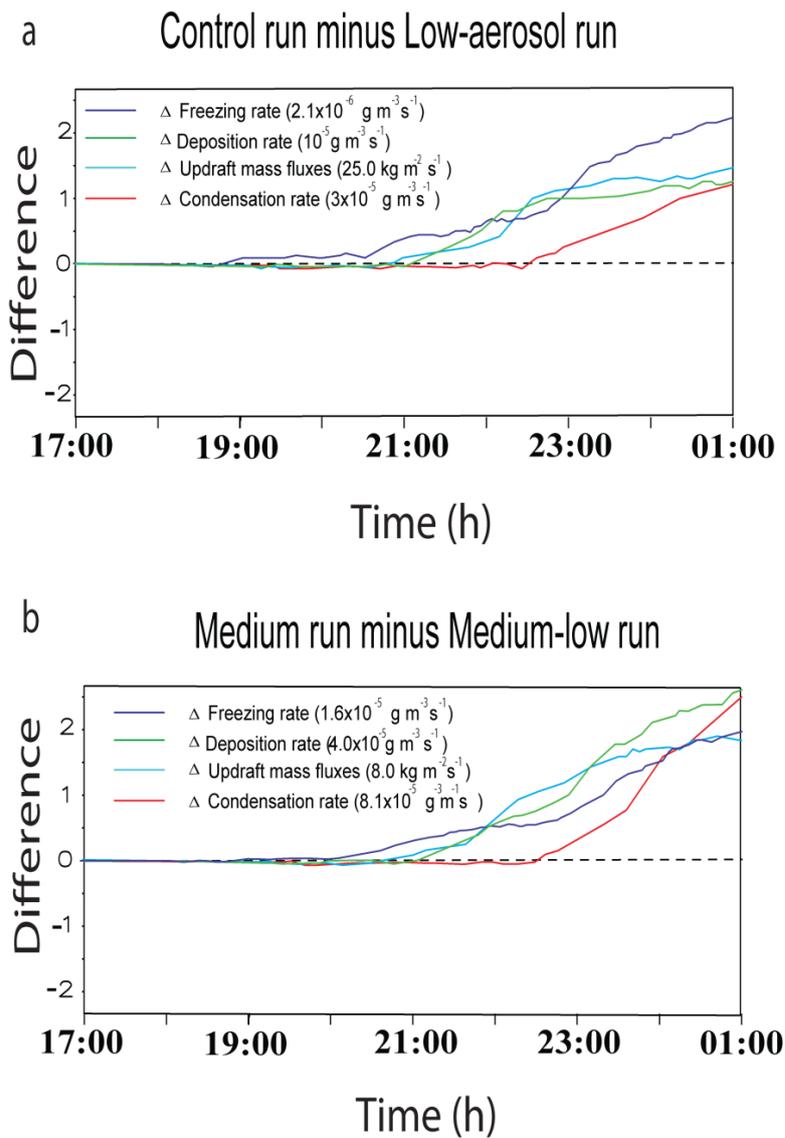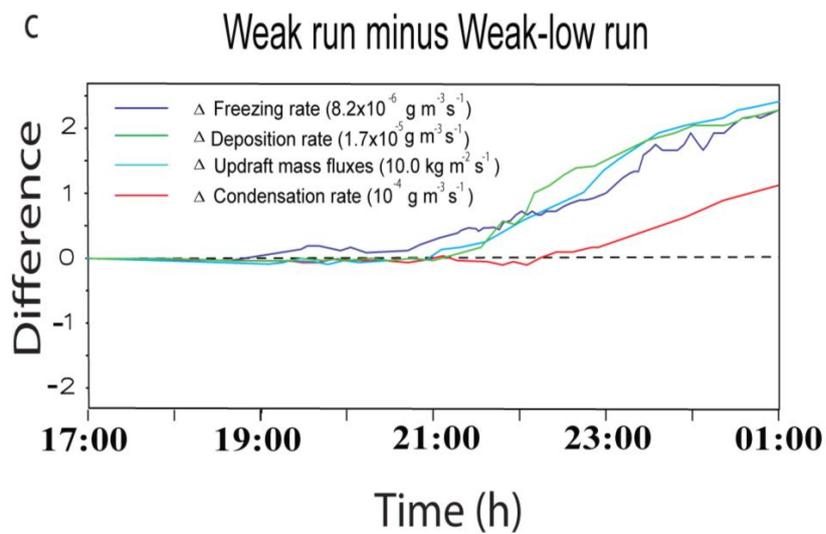
1417

Figure 16

1418

1419

1420

1421

1422

1423
1424

1425